

JGR Atmospheres

RESEARCH ARTICLE

10.1029/2021JD036003

Key Points:

- Atmospheric moisture can mitigate extreme seasonal excursions, reducing summer temperature maxima on high-obliquity planets
- Latent heat release slows polar cooling, keeping the winter pole warm for longer, and weakening baroclinic eddies and storm tracks
- Combined effects of atmospheric moisture storage and surface heat capacity suggest that high-obliquity planets tend to have weak baroclinicity

Correspondence to:

A. H. Lobo,
ahlobo@uci.edu



Citation:

Lobo, A. H., & Bordoni, S. (2022). The role of water vapor in the response of the extratropical circulation of Earth-like planets to obliquity changes. *Journal of Geophysical Research: Atmospheres*, 127, e2021JD036003. <https://doi.org/10.1029/2021JD036003>

Received 8 OCT 2021

Accepted 23 JUL 2022

The Role of Water Vapor in the Response of the Extratropical Circulation of Earth-Like Planets to Obliquity Changes

Ana H. Lobo^{1,2}  and Simona Bordoni^{1,3} 

¹California Institute of Technology, Pasadena, CA, USA, ²University of California, Irvine, Irvine, CA, USA, ³University of Trento, Trento, Italy

Abstract In this study, we use idealized aquaplanet simulations of Earth-like planets to explore the large-scale atmospheric circulation's response to changes in shortwave radiation, through changes in the planet obliquity, and in longwave radiation, through changes in the prescribed optical depth. We primarily focus on the extratropical circulation and the counterintuitive weakening of extratropical eddy activity, and associated precipitating storm tracks, with increased obliquity. We show that on high-obliquity planets with a small surface thermal inertia, net energy deficit during the winter months is primarily balanced by the latent energy component of the atmospheric heat capacity, which buffers any significant atmospheric cooling. As temperatures finally start to decrease, condensational latent heat release of atmospheric moisture further slows down the cooling and keeps the winter pole warmer than the midlatitudes until after the winter solstice. This prevents vigorous baroclinic eddy activity, which lives off the potential energy stored in the sloping isopycnals, as well as the development of a Ferrel cell and storm track. For planets with larger surface heat capacity, we see a similar suppression, with the energy storage in the ocean surface, rather than atmospheric latent energy storage, primarily balancing the net energy loss during the winter months. These results suggest that, regardless of surface thermal inertia, water-covered high-obliquity Earth-like planets would not experience significant extratropical storm activity and highlight the need for a proper characterization of polar properties in planetary modeling and observational investigations.

Plain Language Summary We explore how global wind patterns and atmospheric energy transport respond to a change in radiation distribution, using a simple general circulation model of an Earth-like planet covered by a thin ocean. We examine changes in both the incoming stellar radiation, through changes in obliquity, and the planet's outgoing thermal radiation, by varying the atmosphere's optical thickness. We focus on the high-latitude effects, where increased obliquity leads to a counterintuitive reduction in eddies. We show that on high-obliquity planets with strong seasonal cycles, water vapor plays a dominant role in the energy budget and serves as a mechanism for storing energy. The energy released from condensation in early winter helps keep the poles warm for several extra weeks, reducing the temperature differences between the high and low latitudes. This leads to smaller values of potential energy available to fuel eddies, which in turn leads to an absence of the Ferrel cell and storm tracks. For planets with a thicker ocean, energy becomes increasingly stored in the ocean surface, rather than in the atmospheric column. These results suggest that, regardless of ocean surface properties, water-covered high-obliquity planets would not experience significant high-latitude storm activity.

1. Introduction

Planetary atmospheric general circulations are driven by top-of-atmosphere radiative imbalances, arising from local differences between the absorbed stellar shortwave radiation and the longwave radiation emitted to space. On long time scales, a local surplus of energy must be compensated with energy export by atmospheric and oceanic circulations toward regions of energy deficit. On shorter time scales, energy storage in the atmospheric column and/or the planetary surface can play a role. Understanding how changes in the energy budget impact the atmospheric circulation and surface climate is a challenge fundamental to atmospheric dynamics and is of increasing interest for exoplanet studies, where top-of-atmosphere radiation is the main observable quantity available for climate characterization.

In this work, we use an idealized general circulation model (GCM) to study the response of the seasonally varying atmospheric circulation of Earth-like planets to changes in shortwave and longwave radiation, and the impact on

surface climate. We build and expand on past work (Lobo & Bordoni, 2020), which focused on the Hadley circulation response to changes in obliquity, to examine the response of the midlatitude and high-latitude circulation. We focus on Earth-like planets because these are attractive observational targets, given that surface liquid water is a minimum requirement for life as we know it. Understanding seasonal features on these planets not only will be essential for a proper characterization of their climate but may also be useful for interpreting temporal variations in observations. Changes in radiation due to planetary obliquity can have a particularly large impact on the seasonal cycle and surface temperatures. There are several examples of high-obliquity planets in our own solar system and, based on models of planet formation, we also expect exoplanets to have a wide range of obliquities (Miguel & Brunini, 2010). Accounting for obliquity, hence, may be essential to fully constrain planetary habitability. Exploring these alternative Earth-like planet configurations is also useful for expanding our understanding of the fundamental dynamics that control Earth's climate. Idealized models are a valuable tool in these investigations, allowing for an exploration of a broad range of planetary configurations and development of a more mechanistic understanding of the relevant physics. They can also, as we explore the vast parameter space of planetary configurations, reveal unusual atmospheric regimes that challenge our understanding of the relevant dynamics.

On Earth, most of the atmospheric energy transport in the tropics is effected by the Hadley cells. In the deep tropics, a significant portion of the total energy transport is due to the ocean (Held, 2001), but we neglect it here. Under equinox conditions, the Hadley cells are roughly hemispherically symmetric, with both ascending branches near the equator. Under solstice conditions, the summer cell becomes weaker and the winter Hadley cell strengthens and expands, in response to the insolation peak moving poleward (Lindzen & Hou, 1988), as also happens with increased obliquity (Figures 1a and 1c). However, the Hadley cell is dynamically constrained and cannot expand beyond the midlatitudes at Earth's rotation rate (Faulk et al., 2017; Guendelman & Kaspi, 2019; Held & Hou, 1980; Kaspi & Showman, 2015) even with extreme insolation changes (Guendelman & Kaspi, 2018; Lobo & Bordoni, 2020). Thus, increased radiative imbalances at the poles, beyond the winter Hadley cell's reach, require additional changes in atmospheric circulations other than the Hadley cells.

The dynamical constraints on the Hadley cell have an important impact on the hydrological cycle, for instance determining the position of the region of most intense tropical precipitation within the intertropical convergence zone (ITCZ). Lobo and Bordoni (2020) showed that in high-obliquity simulations, the ITCZ remains in the midlatitudes, as does the ascending branch of the winter Hadley cell in solstitial seasons, even if near-surface temperature and moist static energy (MSE) maximize at the summer pole. They also discussed important features of the hydrological cycle outside the latitudes spanned by the Hadley circulations. At the poles, nonnegligible precipitation is seen during the summer season. This is driven by small-scale convection over the near-surface MSE maximum early in the summer, and by large-scale condensation at the end of the summer. Moisture budget analyses revealed how this arises from rapid variations in the atmospheric water holding capacity due to rapid decreases in temperature at the end of the warm season. The lack of a storm track in the winter hemisphere was also noteworthy.

Storm tracks, bands of enhanced precipitation particularly evident in the extratropics of the winter hemisphere, are associated with moisture flux convergence by large-scale baroclinic eddies, fueled by available potential energy in regions of large isentropic slope. The isentropic slope is directly proportional to horizontal temperature gradients and inversely proportional to dry static stability (e.g., O'Gorman & Schneider, 2008). The role of horizontal temperature gradients is well documented (Peixoto & Oort, 1992; Pierrehumbert & Swanson, 1995; Schneider & Walker, 2006; Stone, 1978), and the combined effects of temperature gradients and dry static stability on isentropic slope can be quantified with the mean available potential energy (MAPE) framework (O'Gorman & Schneider, 2008). Storm track intensity and position can vary significantly throughout the season, as temperature gradients shift in position and/or magnitude. One would expect that large solstitial meridional insolation gradients would lead to strong meridional temperature gradients and enhanced eddy activity. However, high-obliquity simulations with idealized GCMs (Ferreira et al., 2014; Guendelman & Kaspi, 2018; Lobo & Bordoni, 2020) where the solstitial pole-to-pole insolation gradient is maximized indicate a significant strengthening of the winter Hadley cell but a surprising general reduction of baroclinic eddy activity, particularly around the winter solstice. This results in a weakening or absence of the storm tracks and of the winter Ferrel cell.

The relationships between radiative forcings, surface climate, and the atmospheric circulation are complex and include many nonlinear interactions. Some of the strongest nonlinearities in the climate system are associated with atmospheric water vapor, which has a strong nonlinear dependence on temperature through the Clausius–

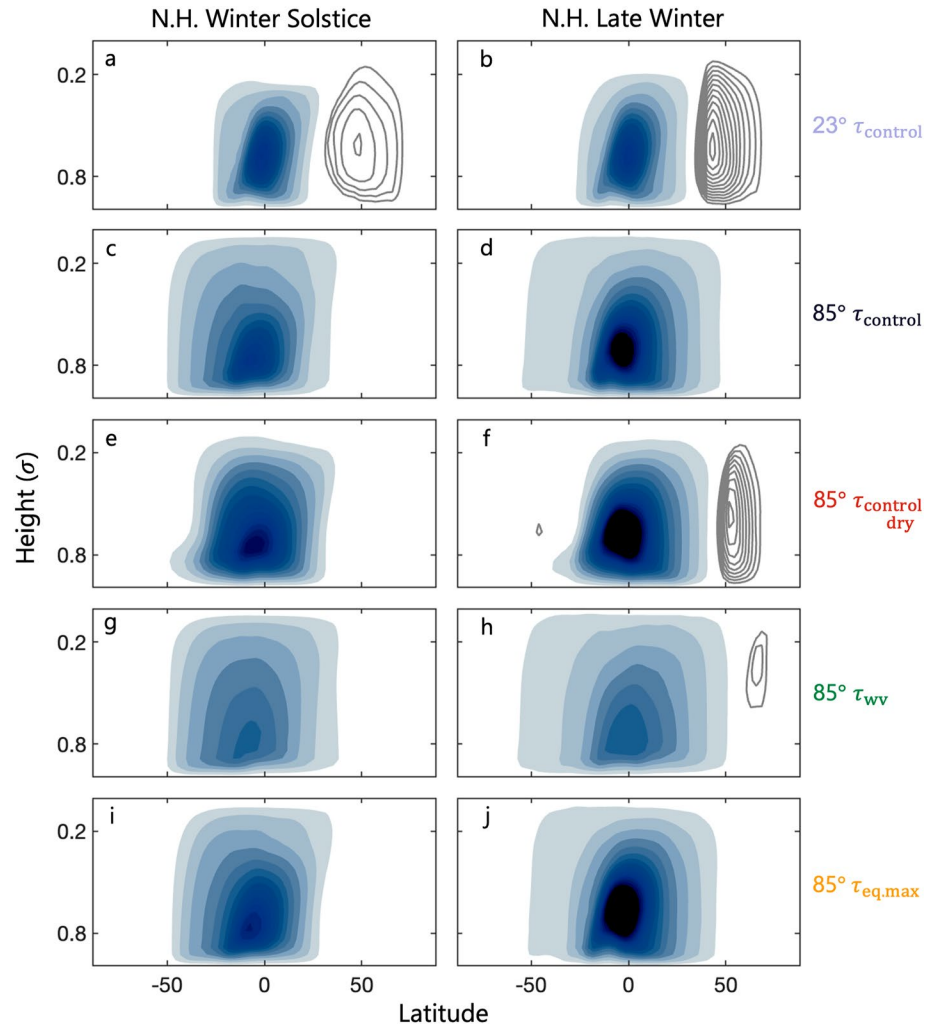


Figure 1. Contours of mass flux stream functions during NH winter solstice (day 270, left) and late winter (day 330, right). Color contours show the clockwise winter Hadley cell, with intervals of 5×10^{10} kg/s. Gray lines show stream function for the counterclockwise winter Ferrel cells, with intervals of 5×10^9 kg/s and a minimum cutoff of 10^{10} kg/s. The top two rows show simulations with constant optical depth (τ_{control}), at 23° (a, b) and 85° (c, d) obliquity. The middle row (e, f) shows results from a dry simulation. The bottom rows show 85° obliquity with a water-vapor-dependent optical depth (τ_{wv} , g, h) and a latitudinally varying optical depth ($\tau_{\text{eq,max}}$, i, j).

Clapeyron relation. More specifically, water vapor can impact the surface climate, especially when seasonal cycles are considered, through a number of pathways: (a) it is a potent greenhouse gas, exerting a strong positive radiative feedback (e.g., Held & Soden, 2000); (b) it undergoes phase transitions, with the associated latent heat release/absorption having direct and indirect impacts on the temperature distribution, the atmospheric circulation, and the hydrological cycle in both the tropics and the extratropics (e.g., Feldl et al., 2017; Lobo & Bordoni, 2020; Neelin & Held, 1987; O’Gorman, 2011; Pfahl et al., 2015); (c) it can alter the effective heat capacity of the atmospheric column (e.g., Cronin & Emanuel, 2013), thus exerting an impact on the response to any seasonally varying forcing.

In this paper, we expand on our previous work in Lobo and Bordoni (2020) and we study the response of the extratropical atmospheric circulation to changes in both shortwave and longwave radiation. We are particularly interested in the seasonally varying response of the wintertime baroclinic eddies and how this relates to the surface and atmospheric temperature distribution. We interpret our results using the MSE budget, which has been extensively used in the literature to understand the response of important features of the tropical mean meridional circulation, including the ITCZ position, to perturbations on different time scales (e.g., Bischoff &

Schneider, 2014; McGee et al., 2014; Neelin, 2007; Neelin & Held, 1987) and which has recently been extended to the understanding of Earth's storm track shifts (Barpanda & Shaw, 2017, 2020). The MSE budget has the appeal of interpreting the tropical and extratropical atmospheric circulations (including baroclinic eddies) as part of the global energy budget and relating them to sources and sinks of energy through the top and the bottom of the atmospheric column, as well as atmospheric and surface energy storage. By applying this framework to the understanding of the seasonality of zonal-mean storm tracks in aquaplanet simulations at Earth's obliquity, Barpanda and Shaw (2020) for instance showed how a large heat capacity of the lower boundary buffers insolation through surface fluxes, resulting in small seasonality of the net energy input (NEI) and, with it, of the storm tracks, as for instance seen in Earth's Southern Hemisphere. For small mixed layer depths, they found a large seasonality of the NEI, which leads to a large storm track seasonality, but also an increasing role for atmospheric energy storage. Here, we expand their analyses to consideration of more extreme seasonal cycles as obliquity is increased and we expose mechanisms by which atmospheric energy storage influences the resulting storm tracks by its influence on atmospheric temperature seasonality. The paper is organized as follows: we begin in Section 2 with a description of the GCM and an overview of the numerical simulations. We then examine the response of the extratropical atmospheric circulation to obliquity-induced changes in the seasonally varying shortwave radiation, and to the presence or absence of moisture in Section 3. In Section 4, we study the influence of perturbations in the longwave radiation, while in Section 5 we explore the sensitivity of our results to changes in surface heat capacity. Discussions and conclusions follow in Section 6.

2. Methods

We use an idealized GCM of an ideal-gas atmosphere (Frierson et al., 2007; O'Gorman & Schneider, 2008), with the setup described in Lobo and Bordoni (2020). The model uses a two-stream gray radiation scheme and a 360-day seasonal cycle of insolation. The GCM is a moist model, which includes an active hydrological cycle, where precipitation can form through either grid-scale condensation or convection, following a simplified quasi-equilibrium convection scheme (Frierson et al., 2007; O'Gorman & Schneider, 2008). The model is run with a uniform slab ocean of constant depth (aquaplanet) and constant surface albedo of 0.38, which in the control configuration yields global mean surface temperatures representative of Earth's present-day climate. In the configuration used here, there is no ocean heat transport.

To explore the response of the atmospheric circulation to radiative perturbations, we run simulations with changes to both the prescribed shortwave radiation and longwave optical depth. Changes in shortwave radiation are introduced by varying the planetary obliquity, with values equal to 23°, 40°, 54°, 70°, and 85°. For obliquities larger than 54°, over the course of a year the planet receives on average more energy at the poles than at the equator (e.g., Ferreira et al., 2014; Ohno & Zhang, 2019a). Changes in longwave are obtained by varying the latitudinal structure of the optical depth, at both 23° and 85°. More specifically, in the control runs the prescribed longwave optical depth of the atmosphere is constant with latitude and only varies vertically as a function of pressure (simulations with this setup will be referred to as τ_{control}). The vertical structure reproduces a well-mixed CO₂-like absorber and a bottom-heavy water vapor-like absorber:

$$\tau(p) = \tau_o \left[f \left(\frac{p}{p_0} \right) + (1 - f) \left(\frac{p}{p_0} \right)^4 \right], \quad (1)$$

where $\tau_o = 4.57$ and $f = 0.2$. Given that τ is fixed and independent of water vapor concentration, there is no water vapor feedback.

We perform additional simulations in which the prescribed optical depth is also a function of latitude, maximizing at the equator and minimizing at the poles (which will be referenced as $\tau_{\text{eq,max}}$), according to

$$\tau_o = \tau_{o_{\text{eq}}} + (\tau_{o_{\text{pole}}} - \tau_{o_{\text{eq}}}) \sin^2(\phi), \quad (2)$$

where ϕ is latitude, $\tau_{o_{\text{eq}}} = 7.2$, and $\tau_{o_{\text{pole}}} = 1.8$. These are the same values as those used in O'Gorman and Schneider (2008) to study the annual mean atmospheric circulation on Earth. $\tau_{\text{eq,max}}$ has an optical depth lower than τ_{control} poleward of 45° latitude.

We also include simulations where the optical depth varies over time according to the local water vapor concentration (which will be referenced as τ_{wv}), thus providing a simple representation of the water vapor feedback (Merlis & Schneider, 2010), with the optical depth modified as

$$\tau(p) = \tau_o \left(\frac{p}{p_0} \right) + \tau_{o_{\text{wv}}} \left(\frac{p}{p_0} \right)^4, \quad (3)$$

where $\tau_{o_{\text{wv}}}$ is the vertically integrated specific humidity, divided by an empirical constant (in this study 98 Pa) chosen so that $\tau_{o_{\text{wv}}}$ remains order 1. τ_o is set to 1.39.

All of the parameters in the different optical depth formulations were chosen so that at 23° obliquity, they result in approximately the same planetary global mean temperatures. Thus, we are focusing on the effects of a spatial redistribution of energy, rather than an overall warming or cooling. For comparison, we also show “dry” runs at 23° and 85° obliquity. These simulations have the same optical depth as in τ_{control} , but the saturation vapor pressure is prescribed to be zero everywhere (as in Frierson et al., 2007), thus eliminating the atmosphere’s ability to store or transport water vapor and any effect related to condensational latent heat release.

The use of a gray radiation scheme in a well-documented and extensively used idealized GCM is a convenient tool that facilitates our study of fundamental dynamical processes, but we should caution that such a simplified setup is not able to, nor intended to, fully reproduce observations even in traditional terrestrial cases. As quantified by Tan et al. (2019), gray radiation schemes can result in enhanced stratospheric temperature gradients, split jet patterns, and a nonmonotonic shift in eddy latitude in response to global planetary warming. For the purposes of this planetary study, we do not consider these effects to be of leading order, especially given that we do not seek to quantify changes in the positions of storm tracks or jets in Earth’s climate. Many of the differences in the gray radiation scheme’s response to warmer climates, compared to more complex radiation schemes, follow from the lack of an interactive water vapor feedback. As we shall show, water vapor indeed plays a key role in our simulations and we intentionally contrast a control run, which lacks an interactive water vapor feedback, with the dry and τ_{wv} simulations to isolate water vapor’s impact on the extratropical circulation through the energy budget. We hence argue that, despite its limitations, the model used here captures the essential dynamics of processes that mediate the response of Earth-like planets to obliquity changes, and we leave to future work investigations with more complex treatments of radiative transfer.

Given that we are particularly interested in the seasonal cycle, we use a shallow mixed layer depth of 1 m for most simulations. This is equivalent to a heat capacity of $4.13 \times 10^6 \text{ J m}^{-2} \text{ K}^{-1}$ and a thermal inertia timescale of ~ 1 day (Cronin & Emanuel, 2013). These conditions result in more extreme seasonal variations than we would expect for an ocean-covered surface on Earth, which helps isolate mechanisms behind the seasonal changes. Given that surface heat capacity impacts the midlatitude and storm track energetics (Barpanda & Shaw, 2020; Donohoe et al., 2014), we also briefly address the effects of increased surface heat capacity, with results from 85° obliquity simulations with a mixed layer depth of 10, 25, and 50 m. The simulations with increased mixed layer depth more closely represent a planet with an ocean-covered surface, with thermal inertia timescales of up to 2 months.

All remaining planetary and orbital parameters are given Earth-like values (as listed in Lobo & Bordoni, 2020). For simplicity, we only consider planets with Earth’s rotation rate in this paper, though we note that for different rotation rates the separation between tropical and extratropical dynamical regimes would shift in latitude (see Showman et al., 2013), such that very slow rotating planets would be “all-tropics” planets (Mitchell et al., 2009), with global Hadley cells (Faulk et al., 2017; Guendelman & Kaspi, 2019; Kaspi & Showman, 2015).

3. Response to Changes in Shortwave Distribution

We begin by studying the planetary circulation response to obliquity-induced changes in the insolation forcing. Incoming stellar radiation is a prescribed model quantity, and its intensity is easily observable for most planetary systems. Varying the magnitude through changes in orbital radius (e.g., Kaspi & Showman, 2015) or radiative profile (e.g., Wolf et al., 2017) can significantly alter surface climate. But changes in the insolation meridional distribution are also capable of shaping a planet’s climate in important ways. As a simple means to examine the influence of the insolation spatial distribution, we shall consider simulations where obliquity is varied between

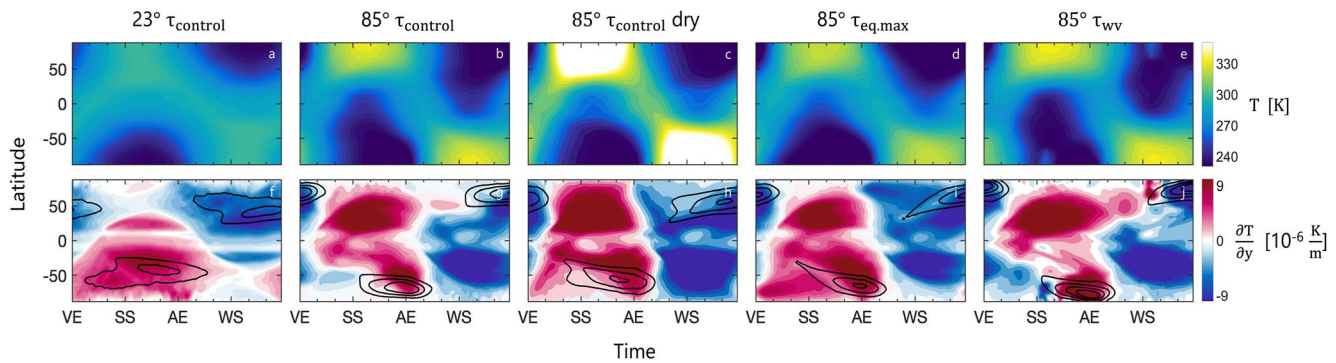


Figure 2. Near-surface temperatures (top row), and meridional temperature gradient (bottom row) for simulations with different obliquities and optical depth structures: from left to right, 23° τ_{control} , 85° τ_{control} , 85° τ_{control} dry, 85° $\tau_{\text{eq,max}}$, and 85° τ_{wv} . The x-axis shows time starting from Northern Hemisphere vernal equinox (VE), with other tick marks indicating summer solstice (SS), autumnal equinox (AE), and winter solstice (WS). The black contours (bottom row) show regions of positive (negative) vertically integrated meridional temperature gradients in the Southern (Northern) Hemisphere with intervals of 5 × 10⁻⁶ K/m.

23° (Earth-like) and 85°. In the high-obliquity cases, summer insolation has a single maximum at the poles and on the annual average more energy is delivered to the poles than to the equator.

Obliquity-induced changes in the seasonal insolation distribution manifest corresponding changes in surface temperatures (Figure 2), which tend to follow the insolation pattern albeit with a lag of about a month. Given the small thermal inertia of the lower boundary, this lag arises from atmospheric dynamic and thermal inertia. Not surprisingly, relative to the low-obliquity cases (Figure 2a), the high-obliquity simulations (Figures 2b–2e) feature more extreme polar temperatures, with very high temperatures during the summer and very cold temperatures during the winter. Hence, the poles in high-obliquity simulations experience a much larger range of temperature throughout the seasonal cycle.

However, the temperature contrast between the summer and winter hemispheres is weaker than we would expect from radiative equilibrium, due in part to the strong cross-equatorial energy transport by the winter Hadley cell, which significantly broadens and strengthens with increasing obliquity (Figure 1). This results in increased energy transport toward the winter hemisphere, as the Hadley cell tends to transport energy in the direction of its upper-level mass transport. Comparing the low-obliquity simulation (23° τ_{control}) to the high-obliquity case (85° τ_{control}), we can observe how the winter Hadley cell edges broaden from ~30° latitude in either hemispheres at 23° obliquity to ~60° latitude at high obliquity. Despite this significant broadening, the cell is not global even in the highest obliquity case (see Figure 9 in Lobo & Bordoni, 2020).

Given that the Hadley cell does not become truly global, it might seem surprising that in the high-obliquity control simulations, there is no evidence of a Ferrel cell in the winter hemisphere (Figures 1c and 1d). We might expect that the strong solstitial insolation gradients at high obliquities, which result in a strengthening of the low-latitude MSE transport, would result in a similar strengthening of the high-latitude eddy transport and a corresponding intensification of the winter Ferrel cell. But, while we see a strong winter Ferrel cell for 23° obliquity, both in midwinter and late winter (Figures 1a and 1b), it is entirely absent for 85° τ_{control} .

3.1. Eddy Activity

The absence of the Ferrel cell, and with it the absence of a precipitation storm track, in the high-obliquity simulations results from a progressive reduction in eddy activity as obliquity increases. This reduction was previously noted in Lobo and Bordoni (2020), which showed that increasing obliquity from 23° to 85° leads to a monotonic decrease in winter eddy kinetic energy (EKE). Here, we examine in detail its seasonal evolution across simulations. In particular, Figure 3 shows vertically integrated EKE values averaged over the northern hemisphere (NH) midlatitudes and high latitudes (between 35° and 90°N). We average over a relatively broad meridional band to capture baroclinic eddy activity, which shifts poleward with increasing obliquity, across the various simulations. As obliquity is increased, in addition to the EKE weakening, we also see changes in its seasonality, with a weakened, delayed, and shorter lived maximum. In all of the τ_{control} simulations, the maximum in EKE occurs well after the winter solstice, in fact around boreal vernal equinox, and the timing of the maximum shifts roughly 20 days

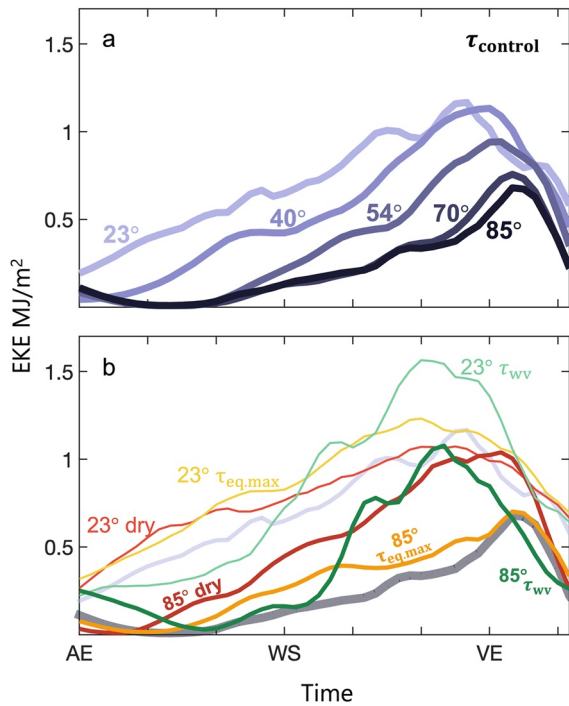


Figure 3. NH winter eddy kinetic energy (EKE), vertically integrated and averaged between 35° and 90° latitude. EKE values are shown over time, measured in days since autumnal equinox and after taking a three-pentad rolling average. The top panel shows τ_{control} results, and the bottom panel shows a variety of configurations at 23° and 85° obliquity. Dry τ_{control} simulations are shown in red, τ_{wv} in green, and $\tau_{\text{eq,max}}$ in yellow, a convention we keep throughout the manuscript.

further from solstice in the 85° obliquity simulation. If we were to choose a threshold to demarcate the start of significant baroclinic eddy activity, for example, 0.5 MJ/m², we would note an even more dramatic delay of roughly 125 days among the control simulations.

Baroclinic eddies form as a result of the vertical shear in the mean flow, sustained through thermal wind balance by the mean meridional temperature gradients. One of the Charney–Stern–Pedlosky necessary conditions for baroclinic instability is that the near-surface vertical gradient of the zonal flow (U_z) has the same sign as the interior potential vorticity gradient. The potential vorticity combines the flow’s relative vorticity, planetary rotation, and a measure of column thickness to describe the absolute circulation of a given air parcel. In the quasi-geostrophic approximation, the potential vorticity (q) can be written as

$$q = \beta y + \nabla^2 \Psi + \frac{\partial}{\partial z} \left(\frac{f^2}{N^2} \frac{\partial \Psi}{\partial z} \right), \quad (4)$$

where β is the meridional gradient of the Coriolis parameter (f), and N^2 is the Brunt–Väisälä frequency. In our simulations, the meridional PV gradient q_y is dominated by the beta effect and is positive. Based on thermal wind, this implies that the necessary condition for baroclinic instability during NH winter is that the meridional temperature gradient is negative. We can confirm that this is the case by examining the top panels in Figure 4, which show vertically integrated meridional temperature gradients (color contours) and EKE (black contours) throughout the NH winter. Though not identical, in these simulations vertically integrated and near-surface temperature gradients have qualitatively similar temporal and spatial patterns, as can be noted in Figures 2 and 5. For a simplified description, they can be used somewhat interchangeably. However, here we use vertically integrated temperature gradients because of their relation to MAPE, as discussed below. For 23° obliquity, extratropical meridional temperature gradients become predominantly negative just before boreal autumnal equinox (Figure 4a) and eddy activity increases shortly after as the gradients intensify. For 85° obliquity, the necessary condition for instability is only met briefly at the end of the winter, after the solstice, and baroclinic eddy activity is only sustained during the short time interval in which gradients remain negative (Figure 4b).

For 85° obliquity, the necessary condition for instability is only met briefly at the end of the winter, after the solstice, and baroclinic eddy activity is only sustained during the short time interval in which gradients remain negative (Figure 4b).

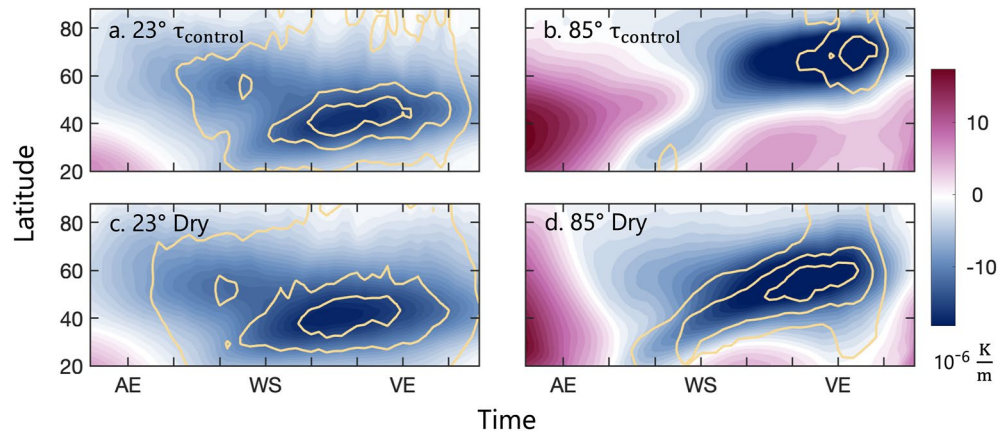


Figure 4. Vertically integrated meridional temperature gradients (K/m, color contours) and vertically integrated eddy kinetic energy (EKE; intervals of 0.5 MJ/m², line contours) during NH winter. The panels show values for 23° (left) and 85° (right) simulations, both with τ_{control} (top) and τ_{control} dry (bottom) configurations.

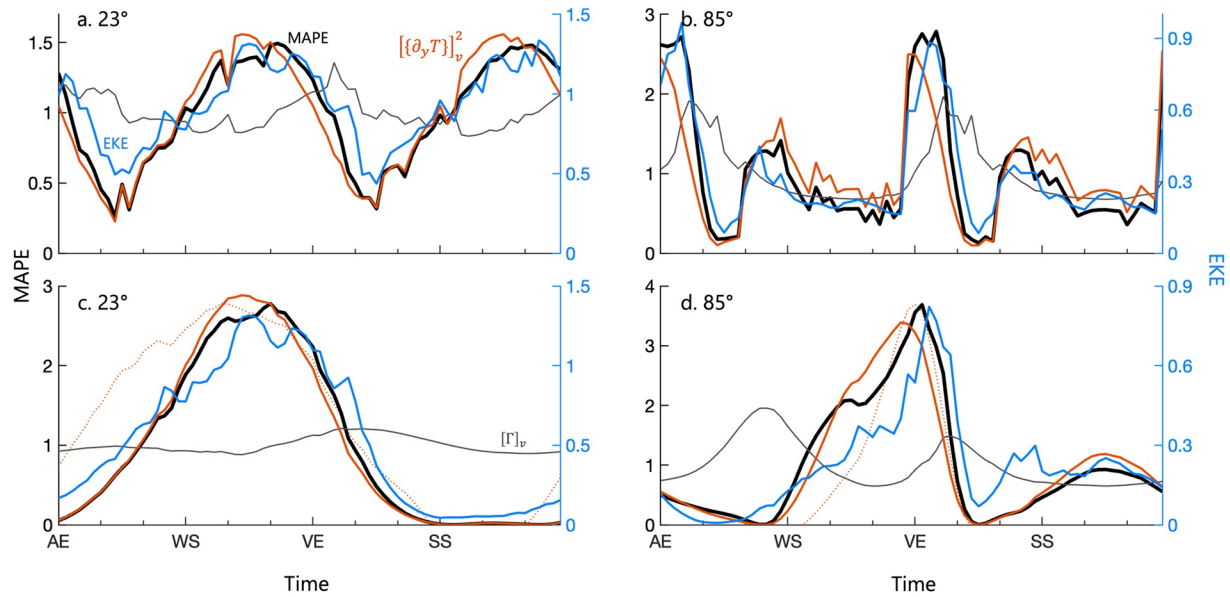


Figure 5. Comparison of mean available potential energy (MAPE) and eddy kinetic energy (EKE) values in the 23° (left) and 85° (right) τ_{control} simulations throughout the year. Top row shows values averaged across the baroclinic zone which varies position with time, and the bottom row shows values averaged over a fixed latitude band centered on the latitude of the yearly eddy potential temperature flux maximum in the Northern Hemisphere. The left y-axis shows values of MAPE (black), meridional temperature gradients $[\{\partial_y T\}]_v^2$ (red), and inverse dry static stability $[\Gamma]_v$ (gray), all expressed as a fraction of their annual mean value. For comparison, we also show near-surface temperature gradients in panels (c) and (d) (red dotted line), plotted as $[-\partial_y T_{sf}]$ to highlight the time period when temperature gradients are negative in the NH. Values below zero are cutoff by the y-axis, and the magnitude is scaled so that the peak matches the MAPE maxima. The right y-axis shows EKE values in MJ/m^2 (blue).

Given the Charney–Stern–Pedlosky condition, we can use near-surface meridional temperature gradients as a minimum condition for instability. However, a more complete description of baroclinic conditions ought to include a measure of vertical atmospheric stratification, given that eddies are fueled by the potential energy stored in isopycnal slopes. This can be obtained by examining the MAPE, using the approximate definition proposed by O’Gorman and Schneider (2008). We can further simplify their definition, such that

$$\text{MAPE} \propto [\Gamma]_v [\{\partial_y T\}]_v^2, \quad (5)$$

where Γ is an inverse measure of dry static stability. Using the notation from O’Gorman and Schneider (2008), $[\cdot]_v$ indicates a vertical average from $\sigma = 0.9$ to the tropopause. For simplicity, we ignore variations in tropopause height and integrate up to $\sigma = 0.1$. $\{\cdot\}$ indicates an average over the baroclinic zone, defined as the region within 15° latitude of the maximum vertically integrated eddy potential temperature flux $(\overline{v'\theta'} \cos \phi)$. Note that while the baroclinic zone width remains constant, the location shifts with time and crosses hemispheres. For the high-obliquity case, where there are long periods of weak eddy activity, this results in large jumps in latitude obscuring interpretation. Therefore, we also plot MAPE values averaged over a fixed 30° latitude band centered at the latitude of the yearly eddy potential temperature flux maximum (Figures 5c and 5d). These are 43° and 60° in the 23° and 85° obliquity simulations, respectively.

As we can see in Figure 5, the winter EKE cycle closely follows MAPE, with EKE maxima occurring when temperature gradients are strong and Γ is large (indicative of reduced vertical stability). The increase in $[\{\partial_y T\}]_v^2$ precedes the increase in Γ , both when we examine changes within the baroclinic zone (Figures 5a and 5b) and when we examine values at a fixed latitude band (Figures 5c and 5d). Note that while EKE is a measure of eddy activity, which, during the winter, is dominated by baroclinic eddy activity, it can also include contributions by eddies generated through barotropic instability. This is especially relevant to the extratropical summer (Figure 5d), and as the “baroclinic zone” (as defined for these calculations) crosses through lower latitudes during seasonal transitions (Figure 5b). Therefore, we do not expect EKE values in Figure 5 to ever be exactly zero and we consider values below 0.3 MJ/m^2 to be negligible. For the same reason, we do not expect a close agreement

in the summer (Figure 5d, between SS and AE). That said, for our purpose of examining winter baroclinic eddy activity, timings of “strong” EKE and large values of MAPE are almost coincident, with maxima of the two quantities being only a pentad apart.

Extratropical dry static stability plays a role in determining EKE intensity and favors EKE peaks in the latter half of the winter season in both simulations. During early and midwinter, the absolute value of temperature gradients rise, and Γ decreases, such that $[(\partial_y T)]_v^2$ controls MAPE values. Near vernal equinox, Γ increases as temperature gradients begin to decrease. Since MAPE is a product of both, this results in the MAPE peak lagging slightly behind the peak in $[(\partial_y T)]_v^2$. Therefore, it follows that the EKE peak would also be expected to slightly lag relative to the vertically integrated temperature gradients, as is visible in Figure 5.

For the remainder of this paper, we can significantly simplify our analysis and provide a more intuitive understanding of results, by focusing on the vertically integrated meridional temperature gradients. In other words, the gradient can be thought of as a simple proxy for MAPE. Also, while the definition of MAPE from O’Gorman and Schneider (2008) is indifferent to the sign of the meridional temperature gradient, the time period when temperature gradients reverse signs is necessarily a period of weak temperature gradients. Therefore, we can interchangeably discuss a delay in vertically integrated temperature gradient reversal and a delay in increasing winter MAPE.

3.2. Role of Moisture in the Temperature Seasonal Evolution

What is causing the progressive delay in the timing of the temperature gradient reversal in the high-obliquity simulations? Or, in other words, why does the pole emerging from the summer season cool more slowly when obliquity is large? Note that we focus primarily on the seasonal evolution of high-latitude temperatures because changes in equatorial temperatures are smaller than those at the poles, and no significant shift in the timing of their variations is observed. This is not to say that there are no changes at the low latitudes, but rather that these changes are small compared to those experienced by the polar regions. We will briefly discuss some low-latitude effects in Section 4.

To gain some insight into the different seasonal cycles of temperatures at low and high obliquities, we consider the vertically integrated atmospheric energy budget (e.g., Neelin, 2007):

$$\frac{\partial}{\partial t} \langle \mathcal{E} \rangle + \frac{\partial}{\partial y} \langle \bar{v}h \rangle = R_{\text{toa}} - F_{\text{sfc}}, \quad (6)$$

where $\mathcal{E} = c_p T + L_v q$ is the energy that can be stored in an atmospheric column (neglecting kinetic energy), that is, a moist enthalpy composed of dry enthalpy $c_p T$, with air isobaric specific heat c_p and latent energy $L_v q$, with latent heat of vaporization L_v and specific humidity q ; $h = c_p T + L_v q + gz$ is the MSE, which differs from \mathcal{E} in that it also includes the potential energy gz . Vertical integrals are denoted by $\langle \cdot \rangle$, and $\overline{(\cdot)}$ denotes both a zonal and a temporal long-term pentad average. The first term on the left-hand side represents energy storage in the atmospheric column, while the second term is the divergence of the meridional energy flux $\langle \bar{v}h \rangle = \langle \bar{v}h \rangle + \langle \bar{v}'h' \rangle$, composed of mean and eddy energy fluxes, respectively. The right-hand side of Equation 6 represents the NEI into the atmospheric column, through top-of-atmosphere radiative fluxes R_{toa} and surface radiative and turbulent enthalpy fluxes F_{sfc} .

At lower latitudes, regardless of obliquity value, the dominant balance is between NEI and the MSE flux divergence (Figure 6). However, as obliquity is increased, the NEI can be very large in the high latitudes, with negative values, indicative of energy deficit, in the winter hemisphere, and positive values, indicative of energy surplus, in the summer hemisphere (Figure 6). The weak MSE flux convergence/divergence at these polar latitudes implies an increasing role of the atmospheric energy storage, which include both a dry $\langle \partial_t c_p T \rangle$ and latent $\langle \partial_t L_v q \rangle$ component. Importantly, in a moist atmosphere, changes in NEI are accompanied by changes in latent energy (moisture) in addition to changes in dry enthalpy (temperature). In other words, moisture can buffer temperature changes in response to insolation changes. Figure 6 shows the different terms of the MSE budget at different times of the seasonal cycle for all simulations. Below we will however primarily focus on the behavior of the high-obliquity simulation compared to the low-obliquity simulation, and we will focus on the high latitudes for the reasons articulated above.

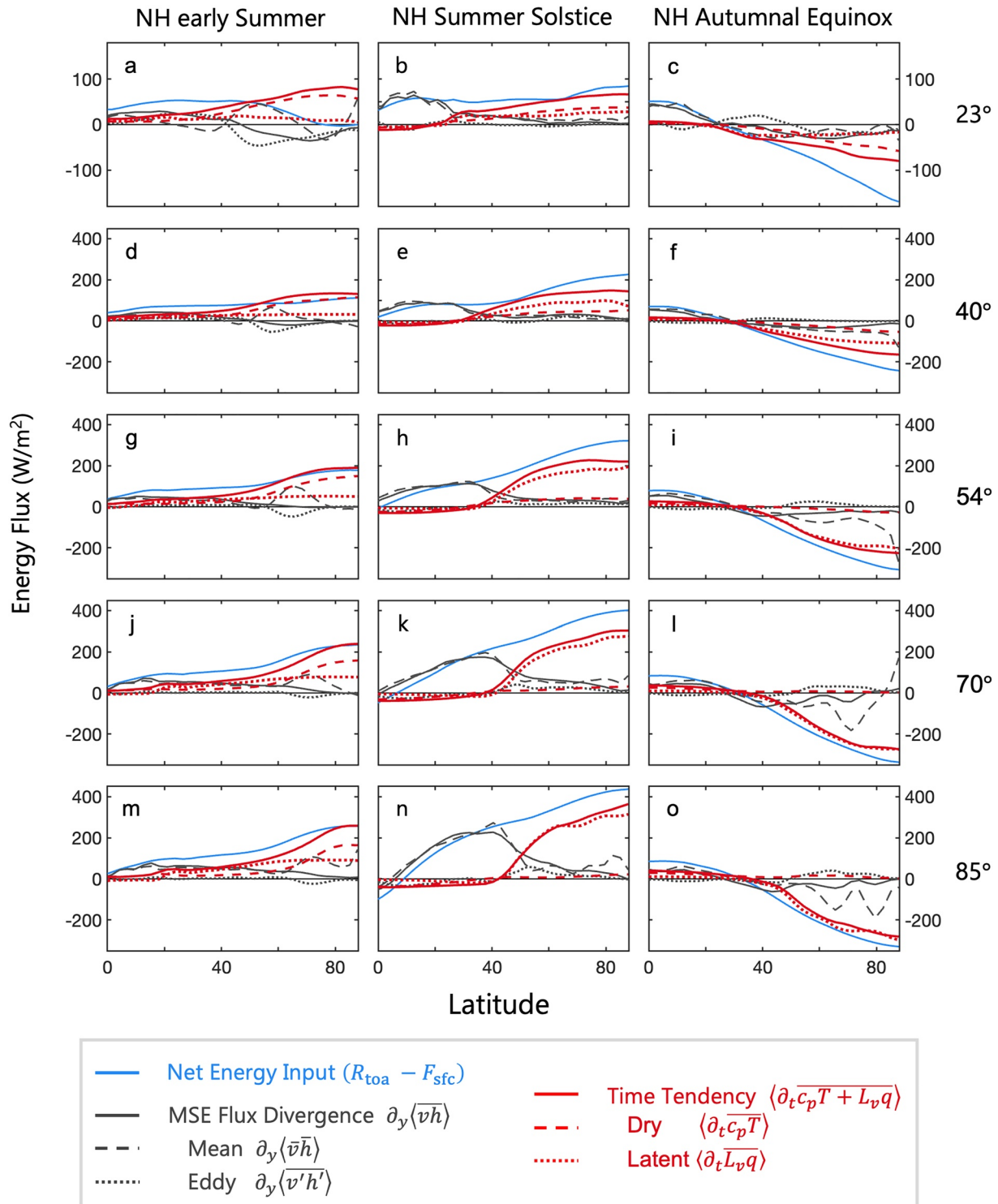


Figure 6. Moist static energy (MSE) budget and role of energy storage during seasonal transitions. The meridional distribution of MSE budget terms in the NH is shown for early summer (40 days after vernal equinox [VE], left), summer solstice (center), and autumnal equinox (right) for all τ_{control} simulations.

As NEI starts increasing in the warm hemisphere after spring equinox, both in the low- and high-obliquity simulations we see an increase in energy storage, initially in the dry component and then, with a slight lag, in the latent energy component as well (Figures 7a and 7c). As summer progresses, the relative contribution of the latent energy storage increases and does more so with higher obliquity: at summer solstice, it is about as large as the

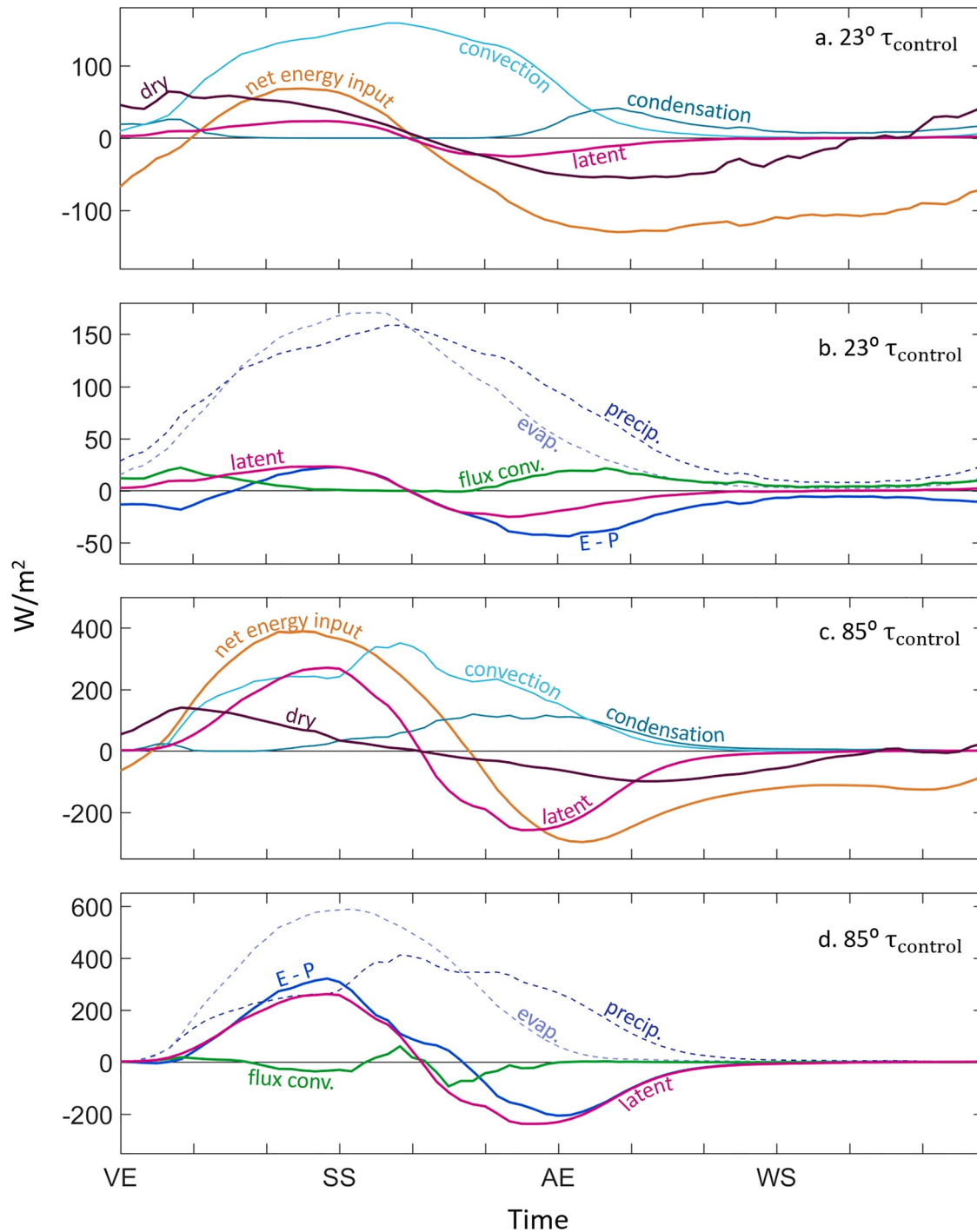


Figure 7. Evolution of energy budget terms (a, c) and moisture budget (b, d) throughout the year for the 23° and 85° τ_{control} simulations. Values show the area weighted average between 60° and 90°N. (a, c) Changes in atmospheric dry (brown) and latent (magenta) energy storage, as well as the net energy input into the atmosphere (orange). Latent heat release from subgrid convection (light blue) and grid-scale condensation (dark blue) is also shown. (b, d) The net evaporation (blue), moisture flux convergence (green), and atmospheric moisture storage (pink). Net evaporation is given by the difference between evaporation (dashed light blue) and precipitation (dashed dark blue).

dry energy storage in the low-obliquity simulation while it is the dominant component in the high-obliquity simulation. By providing an alternative means of energy storage, moisture hence provides a buffering effect on the temperature response to changes in radiative forcing with obliquity, which both reduces the temperature

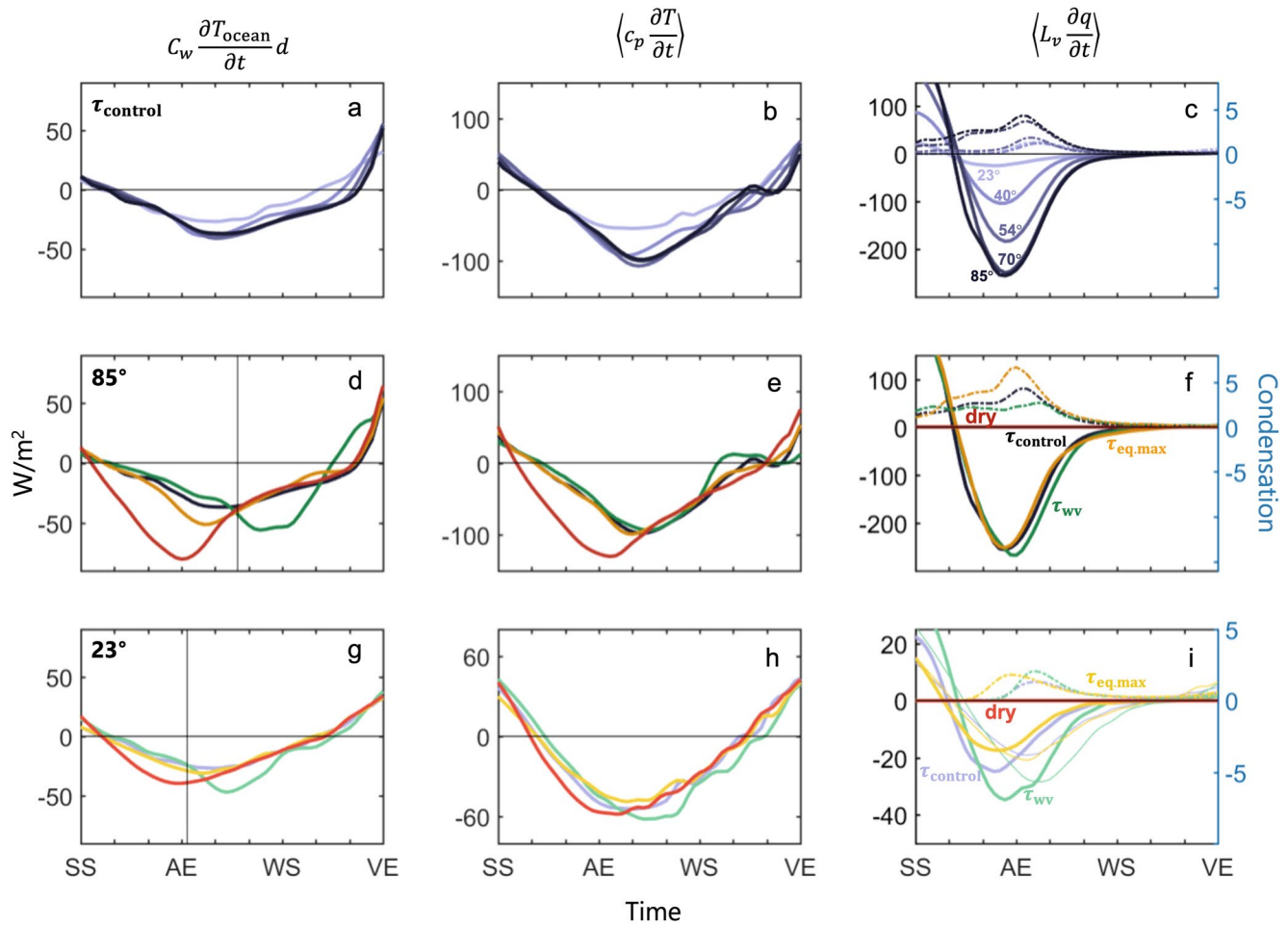


Figure 8. Surface and atmospheric energy storage. Seasonal evolution of the ocean mixed layer energy storage (left), as well as storage in the atmospheric column by dry energy (middle) and latent energy (right, solid lines). Values (W m^{-2}) are vertically integrated, averaged between 60° and 90°N to focus on polar properties, and then smoothed with a three-pentad rolling average. The dash-dotted lines on the right show large-scale precipitation (mm/day). The top row includes only τ_{control} simulations for all obliquity values, while middle and bottom rows include all 85° and 23° simulations, respectively. The vertical lines in panels (d) and (g) show the time when the near-surface high-latitude τ_{wv} optical depth drops below the τ_{control} value. The thin solid lines in panel (i) show change in latent heat between 50° and 20°N . Note that C_w is the specific heat capacity of water, and d is the depth of the ocean mixed layer.

maximum and delays its occurrence relative to the time of summer solstice as obliquity is increased. This delay is about 10 days larger in the 85° than in the 23° case (not shown). The transition from the summer to the winter season reveals even more striking differences between the low- and high-obliquity simulations. In the low-obliquity case, NEI, which becomes negative around 50 days after summer solstice, is primarily balanced by MSE flux convergence and dry enthalpy loss, with latent energy loss playing a negligible role. Significant atmospheric cooling is seen to occur between autumnal equinox and winter summer solstice. At high obliquity, instead, the large and negative NEI around autumnal equinox is primarily balanced by loss of latent energy in the atmospheric column, which reduces and slows down the dry enthalpy loss, which becomes negative only around autumnal equinox and peaks around 50 days later. In other words, latent energy loss at high obliquity also buffers the temperature response in the winter season, slowing down and delaying the cooling due to the negative NEI.

We explore in more detail the behavior of atmospheric energy storage throughout the winter in the high latitudes in Figure 8, which shows the rate at which the vertically integrated atmospheric column is losing dry and latent energy. The dry enthalpy loss increases with increasing obliquity, as does the latent energy, but as discussed above, its relative contribution to the total energy storage decreases. There is also evidence of a delay in the time at which the dry enthalpy reaches its minimum value. The latent energy loss is strongest at equinox, with small variations in timing, but large variations in intensity amongst the simulations, showing a monotonic increase in

magnitude with increased obliquity. The dry enthalpy loss shows a much smaller magnitude increase than the latent energy loss, switching from being the primary means of energy loss in the low-obliquity simulations to playing a more minor role in the high-obliquity simulations.

The role that atmospheric moisture plays in shaping the temperature distribution can be further explored by using the vertically integrated moisture budget, which relates the water vapor storage in the atmosphere to the net evaporation ($E - P$) and convergence of moisture flux by atmospheric motion:

$$\partial_t \langle \bar{q} \rangle = \bar{E} - \bar{P} - \nabla \cdot \langle \bar{q} \bar{\mathbf{u}} \rangle - \nabla \cdot \langle \bar{q}' \bar{\mathbf{u}}' \rangle. \quad (7)$$

The left-hand side represents the storage term, while the right-hand side includes net evaporation, and mean and eddy moisture flux convergence.

All terms of the moisture budget are also shown in Figure 7 for both the 23° and the 85° cases (b and d, respectively). In the 23° simulation (Figure 7b), the small excess evaporation after vernal equinox is balanced by both moisture flux convergence and moisture storage. As the warm season progresses, evaporation grows in excess of precipitation and this is primarily accompanied by an increase in atmospheric moisture (or equivalently in latent energy), which peaks around summer solstice. The large evaporation is driven by large surface temperature and MSE, which sustain some degree of convective activity (Figure 7a). About a month after summer solstice, precipitation starts exceeding evaporation (Figure 7b), which is initially balanced by a decrease in atmospheric moisture, at which time large-scale condensation starts picking up. Near autumnal equinox, however, net precipitation is primarily balanced by eddy moisture flux convergence rather than local condensation. This high-latitude precipitation is however much smaller than the precipitation seen at lower latitudes at the same time and the associated latent heat release is not large enough to compensate the radiative cooling tendency, resulting in dry enthalpy loss and atmospheric cooling lasting from before autumnal equinox throughout winter solstice (not shown).

In the 85° simulation (Figure 7d), we see a much smaller role for moisture flux convergence by the atmospheric circulation and, with the exception of about a month before autumnal equinox, the dominant balance is between moisture storage and net evaporation. Similarly to what is seen in the 23° case, evaporation exceeds precipitation from around vernal equinox to about a month before autumnal equinox, during which time the moisture storage is positive. Differently than the low-obliquity case, however, the high near-surface temperatures and MSE maintain vigorous convection throughout the summer, with precipitation rates smaller than, but of the same order of magnitude of, precipitation rates within the ITCZ (cf., Lobo & Bordoni, 2020). As evaporation rates decrease toward the end of the summer, but the high near-surface temperatures continue to sustain convection, precipitation starts exceeding evaporation about 1 month before autumnal equinox. This is primarily balanced, especially as net precipitation reaches its peak at autumnal equinox, by latent energy loss. Note how the latent heat release associated with both the convective and large-scale precipitation associated with this vigorous convective activity is large enough to compensate for the radiative cooling from summer solstice throughout autumnal equinox, preventing any atmospheric cooling. It is only after autumnal equinox, as convective precipitation rates start decreasing, that cooling radiative tendencies on temperatures are no longer balanced by latent heat release and dry energy loss (and cooling) occurs. In other words, it is only around this time that the latent energy loss is no longer capable of balancing the negative NEI and the dry energy loss is required to achieve energy balance. As discussed in more detail by Lobo and Bordoni (2020), this drop in temperature is accompanied by local condensation of moisture, with large-scale precipitation reaching its peak right after the maximum in latent energy loss (Figure 8c).

We can more directly examine the relationship between latent heat release and temperatures by exploring its contribution to temperature tendencies (Figure 9). Temperature, in fact, changes due to various local energy sources and sinks, including shortwave and longwave radiative fluxes, diffusion, and latent heat release associated with grid-scale condensation, and subgrid scale convection. We group the latter two together and refer to them as $\partial T_{\text{water}} / \partial t$. While large-scale condensation or convection are occurring, latent heat is being released and there is a positive $\partial T_{\text{water}} / \partial t$ in the high latitudes (Figure 9b). We can see that high values of $\partial T_{\text{water}} / \partial t$ in the high latitudes lead to low, or in some cases positive, meridional temperature gradients. In other words, the poles remain warm thanks to the latent heat release. By keeping temperature gradients small or negative, this results in weak baroclinic eddy activity. Then, once the water vapor is sufficiently depleted and the $\partial T_{\text{water}} / \partial t$ term tends to

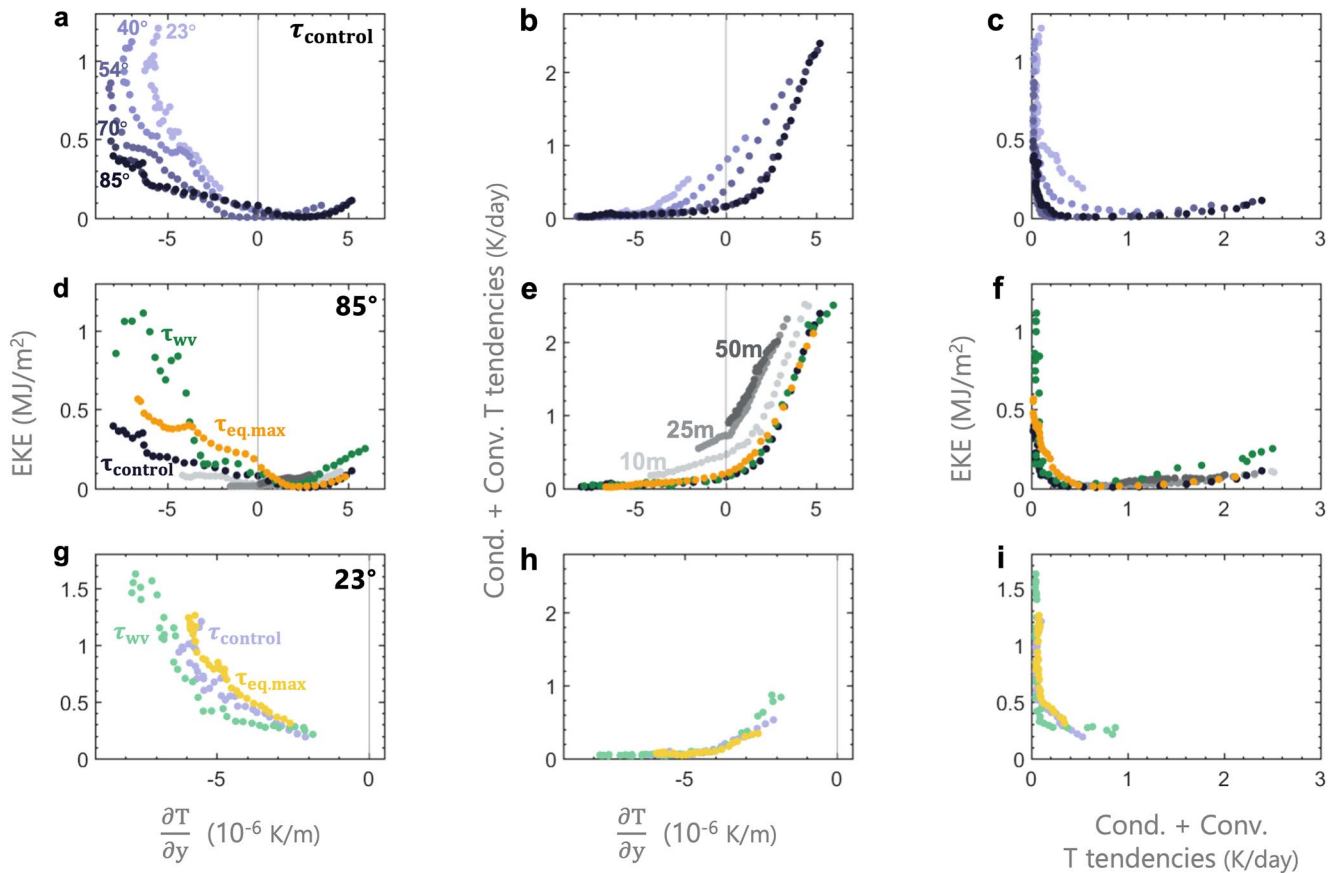


Figure 9. Eddy kinetic energy (EKE) averaged between 35° and 90° latitude versus average meridional temperature gradient (left). High-latitude condensation and convection temperature tendencies versus meridional temperature gradient (center). EKE versus temperature tendencies due to latent heat release (right). All quantities were vertically integrated and averaged over the NH. Each marker shows values from a different pentad during NH winter (from pentad 37 to 71). The simulations used in each row are the same as in Figure 8, but the dry simulations have been removed.

zero, we see a quick increase in negative temperature gradients (Figure 9b) and a sharp rise in EKE. In Figure 9c, we directly compare $\partial T_{\text{water}}/\partial t$ to EKE, which showcases the clear shift that occurs as latent heat release due to water vapor condensation ceases and eddy activity grows.

3.3. Comparison With Dry Simulations

To further illustrate the importance of moisture effects on the temperature patterns and circulation, we compare the control simulations to dry runs where the saturation vapor pressure is set to zero. These dry simulations, at both 23° and 85° obliquity, make it easier to visualize the distinction between the system's thermal inertia and the moisture's buffering effect. As can be noted in Figures 4c and 4d, in the absence of moisture, the meridional temperature gradients reverse near equinox. Similarly, cooling rates are strongest approximately at equinox (Figures 8d and 8e), such that the atmospheric sensible energy loss maximizes roughly 50 days earlier than in the moist simulations.

By affecting the meridional temperature gradients, it is clear that moisture can play a strong role in determining eddy activity. But it is worth briefly considering other mechanisms through which moisture can affect eddies. Latent heat release reduces the atmospheric effective static stability (Chang et al., 2002; Lapeyre & Held, 2004), such that dry models underestimate eddy activity by nearly an order of magnitude if mean fields are held constant (O'Gorman, 2011). Based on that alone, we would expect the moist simulations to have significantly higher EKE values. However, we see that for 85° obliquity the dry simulation has the largest values for EKE, as well as significantly longer duration of winter baroclinic eddy activity (Figure 3). Even for the 23° case, the dry simulation has

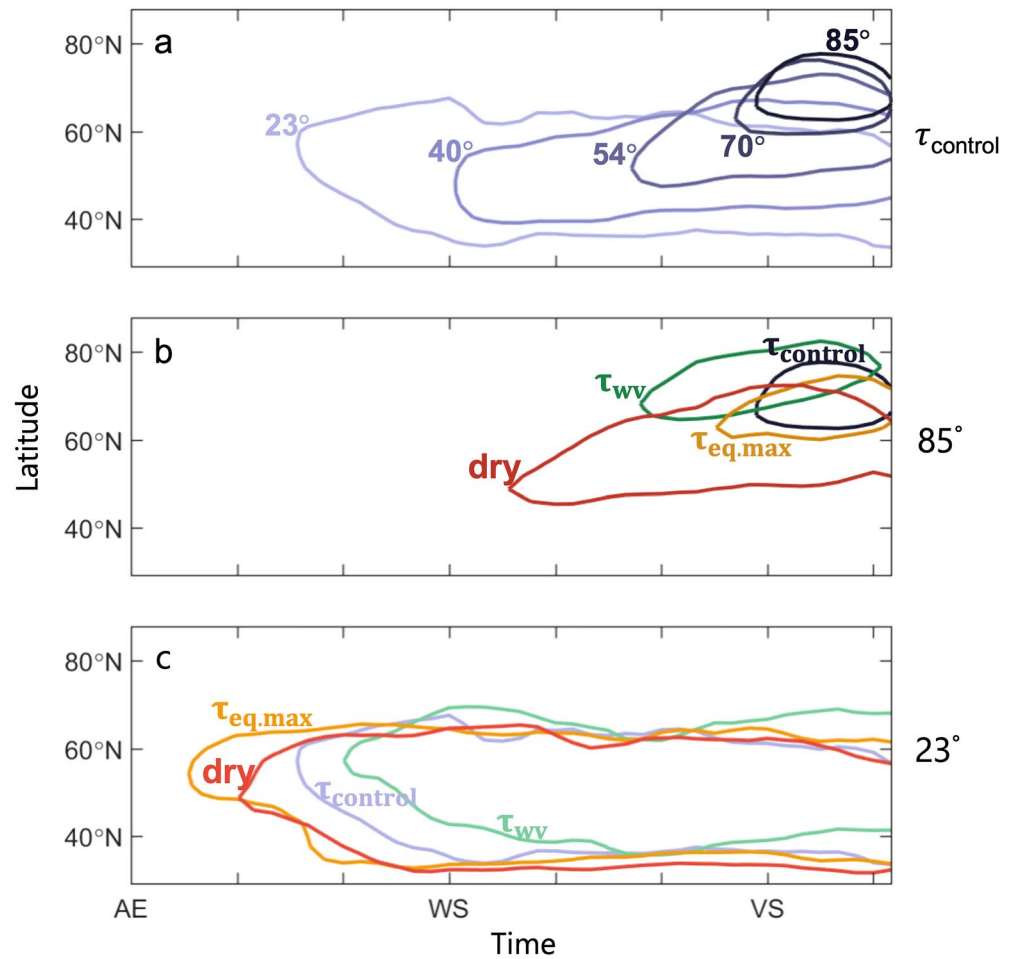


Figure 10. Seasonal evolution of NH Ferrel cell's edge. The cell edge is determined as the latitude at which the vertically integrated stream function exceeds 10^{10} kg/s in magnitude. Colors match previous figures, with (a) showing τ_{control} simulations with various obliquities, (b) 85° simulations, and (c) 23° simulations. We apply the same three-pentad rolling averaging as in previous figures.

slightly larger EKE. This allows us to conclude that the buffering effect is dominant, such that the inclusion of atmospheric water is suppressing rather than enhancing winter baroclinic eddy activity.

As was previously noted, changes in eddy activity also impact the Ferrel cell and storm tracks. For 85° obliquity, the moisture's buffering effect leads to a 70 days delay in the formation of the winter Ferrel cell relative to the dry simulation (Figure 10). Overall, the effects of atmospheric moisture storage on the climate bear many similarities to those of increasing surface heat capacity, which shall be discussed in Section 5. Both mechanisms slow warming during the summer and increase the amount of heat that is available when there is a radiative deficit in the winter, keeping polar temperatures more moderate year-round. In both cases, this leads to a weakening or to the absence of winter baroclinic eddy activity, storm tracks, and winter Ferrel cells.

To summarize, moisture influences the seasonal cycle of high-obliquity planets through the following mechanisms: (a) during early summer, the increase of atmospheric moisture storage slows the rate of warming and reduces and delays temperature maxima. (b) At the end of summer, the negative NEI is primarily balanced by latent energy loss, which delays the atmospheric cooling. (c) The latent energy loss (drying of the atmospheric column) occurs at times when vigorous convective precipitation exceeds evaporation. Significant high-latitude convective activity in high-obliquity simulations results from MSE maximizing at the summer poles. (d) As latent energy loss is no longer able to compensate for the increasingly negative NEI, temperatures start decreasing, which is accompanied by local large-scale condensation of atmospheric moisture. This further extends the high-latitude rainy season to 1 month after autumnal equinox. (e) The steps described above can be reinterpreted

in terms of the positive temperature tendencies due to the diabatic heating associated with high-latitude precipitation. It is the latent heat released as moisture condenses out at times of latent energy loss that gives rise to positive temperature tendencies that counteract the radiatively driven cooling, slowing down polar cooling, and impacting the meridional temperature patterns. For high obliquities, these effects are sufficiently strong to keep the poles warmer than the midlatitudes until winter solstice, delaying or even preventing baroclinic eddy activity, the formation of storm tracks, and the winter Ferrel cell.

4. Response to Changes in Longwave Optical Depth

The intensity of longwave radiation emissions is not a prescribed model quantity and has a complex relationship with the circulation and temperature. However, we can examine the sensitivity of our results to changes in longwave radiation by using different optical depth parameterizations, as described in Section 2. As was the case when we varied obliquity, these simulations were designed to redistribute energy without any net warming or cooling of the planet. In the low latitudes, these various simulations tend to produce qualitatively similar climates. There are some significant changes in overturning intensity and structure that can be noted in Figure 1, but our focus here is on the higher latitudes and on how relatively small changes in longwave optical depth have an impact on eddy activity. Some general patterns can already be discerned by looking at the seasonal evolution of the EKE across these optical depth simulations (Figure 9). The EKE maximum is larger in both the τ_{wv} and the $\tau_{\text{eq,max}}$ simulations than in the τ_{control} simulations, regardless of obliquity. In terms of timing, the results show a less clear tendency, with different formulations leading to a smaller or larger delay depending on the obliquity value. This can also be noted in the seasonal evolution of the Ferrel cell's edge in Figure 10.

In simulations with latitudinally varying optical depth ($\tau_{\text{eq,max}}$), the atmosphere is optically thicker (thinner) at the equator (pole). At high obliquity, this results, as might be expected, in a cooler polar summer (Figure 2d) and also allows for slightly faster cooling during the fall (Figure 8e). This enhanced cooling reduces the polar moisture storage, which in turn leads to a lower maximum in the temperature tendency due to water condensation ($\partial T_{\text{water}}/\partial t$, Figure 9d). As we might expect, in these simulations, high-latitude eddies form slightly more rapidly and achieve higher EKE values than the control simulation. This can be noted in Figure 3 for both high- and low-obliquity cases. The changes in eddy activity are relatively subtle, but can also be noted in the slightly earlier Ferrel cell formation (Figures 10b and 10c).

In the lower-obliquity simulations, changes in midlatitude and low-latitude moisture storage may have an impact on the high-latitude effects we are describing. The high-latitude latent energy variations (solid lines, Figure 8i) are weaker in low-obliquity simulations, such that their magnitude is comparable with the midlatitude variations (thin lines). The latent heat release in the midlatitudes occurs a few weeks later than at the poles and would facilitate more negative temperature gradients during NH winter. Thus, for the $23^\circ \tau_{\text{eq,max}}$ simulation where there is latent heat release in the midlatitudes, combined with a higher optical depth in the low latitudes, it is not surprising that the EKE values surpass those of the τ_{control} simulation (Figure 3). Note that these midlatitude values are not shown in the remaining panels (c and f) because they are very small in comparison to the large polar latent terms of high-obliquity simulations and would be difficult to visualize.

We also consider the effects of a water vapor feedback, which requires the optical depth to vary with time in conjunction with the atmospheric water vapor concentration. During the summer, in the τ_{wv} simulations, temperature increases lead to increased evaporation and increased atmospheric moisture content, which increases the longwave optical depth, establishing a positive feedback. However, once temperatures begin to decrease in the winter and most of the water condenses out, the local optical depth can become lower than in τ_{control} , reducing the greenhouse effect. The time at which the near-surface τ_{wv} polar optical depth (at $\sim 75^\circ$ latitude) drops below τ_{control} is indicated with a vertical gray line in Figures 8f and 8i. The increased high-latitude latent heat effects in τ_{wv} simulations, together with increased summer temperatures, hinders eddy formation in the early winter (Figure 10c). But the accelerated polar cooling later in the season (Figure 8) can facilitate stronger temperature gradients and stronger EKE maxima for τ_{wv} simulations (Figures 3 and 9).

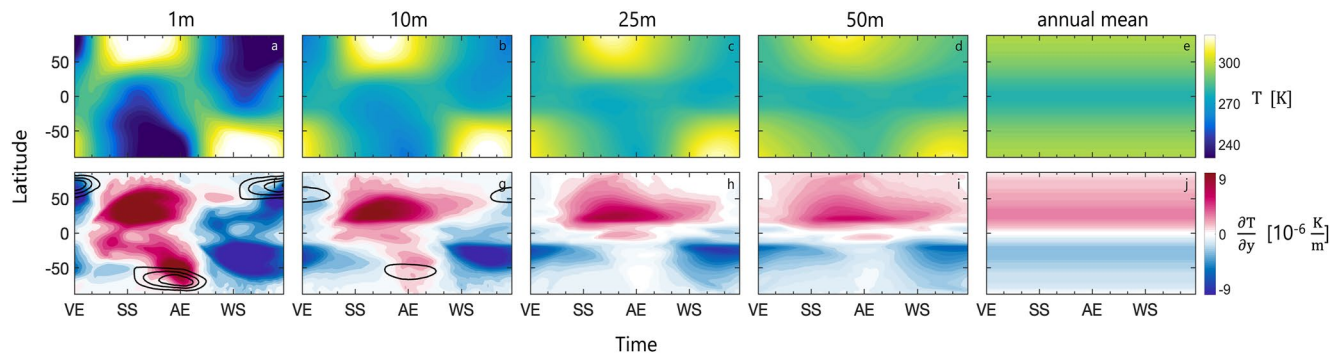


Figure 11. Same as Figure 2 for simulations with 85° obliquity and mixed layer depths increasing from left to right (1, 10, 25, and 50 m). The panels on the far right show a simulation where insolation is kept at its annual mean value. Note that the contour intervals for temperature are different from Figure 2.

5. Response to Changes in Surface Heat Capacity

The effects of atmospheric moisture storage are in many ways similar to the seasonal effects of an increased surface heat capacity. The model's prescribed ocean mixed layer depth determines the surface heat capacity, such that a deeper mixed layer increases the capacity for local energy storage or loss. Increasing the mixed layer depth from 1 to 50 m increases the thermal inertia timescale from about 1 day to about 2 months (Cronin & Emanuel, 2013; Lobo & Bordoni, 2020), reducing the amplitude of seasonal variations in climate. Given that the effects of varying mixed layer depth are well studied for Earth-like (low-obliquity) cases (e.g., Barpanda & Shaw, 2020; Donohoe et al., 2014), here we will primarily focus on high-obliquity simulations with mixed layer depths of 1, 10, 25, and 50 m.

In high-obliquity simulations with a deep mixed layer, the poles remain relatively warm year-round and the meridional temperature gradients in the Northern (Southern) Hemisphere stay positive (negative) most (10 and 25 m) or all of the year (50 m). Increasing the mixed layer depth (Figures 11a–11d) leads, as expected, to behavior increasingly similar to that of simulations forced with annual mean insolation (Figure 11e). In the following, we will only discuss resulting changes in extratropical eddy activity, the main focus of this paper, despite a host of other interesting features emerging outside the polar regions.

As the mixed layer depth is increased, there is an overall reduction of EKE. Focusing on the winter baroclinic eddies, Figure 12 shows that the high-latitude EKE maxima, which appear in the 85° 1 m simulation at the end of winter near vernal equinox, are weaker (10 m), or entirely absent (25 and 50 m) in simulations with deeper mixed layers. The Ferrel cell is similarly absent in these simulations. While in the shallow mixed layer depth simulations, it is primarily atmospheric moisture that prevents the poles from cooling during the winter, through its buffering effect and the associated latent heat release upon condensation, in the deeper mixed layer depth simulations energy exchanges with the surface play an increasingly dominant role. This can be seen both in the influence of latent heat release upon condensation on temperature gradients (Figure 9e), which decreases as the mixed layer depth increases, and in the relative magnitude of the surface and atmospheric energy storage (Figure 13): already at intermediate mixed layer depths (10 and 25 m), surface heat exchanges dominate over atmospheric energy storage terms. It is indeed the buffering effect of the surface heat capacity, with the ocean uptaking heat during the summer and releasing it during the winter, which prevents large temperature excursions at the high latitudes

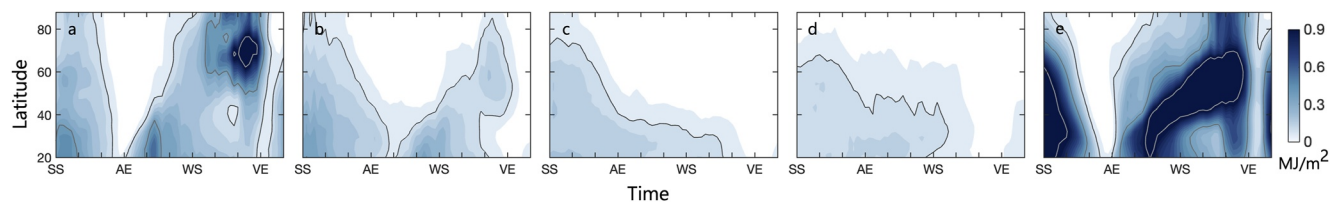


Figure 12. Vertically integrated eddy kinetic energy (EKE), for 85° obliquity moist simulations with varying mixed layer depth (1, 10, 25, and 50 m, from left to right). For comparison, the far right panel shows values for the dry 85° 1 m mixed layer depth simulation. Gray lines highlight EKE values of 0.1 (dark gray), 0.4 (medium gray), and 1 MJ/m² (light gray) to facilitate comparisons.

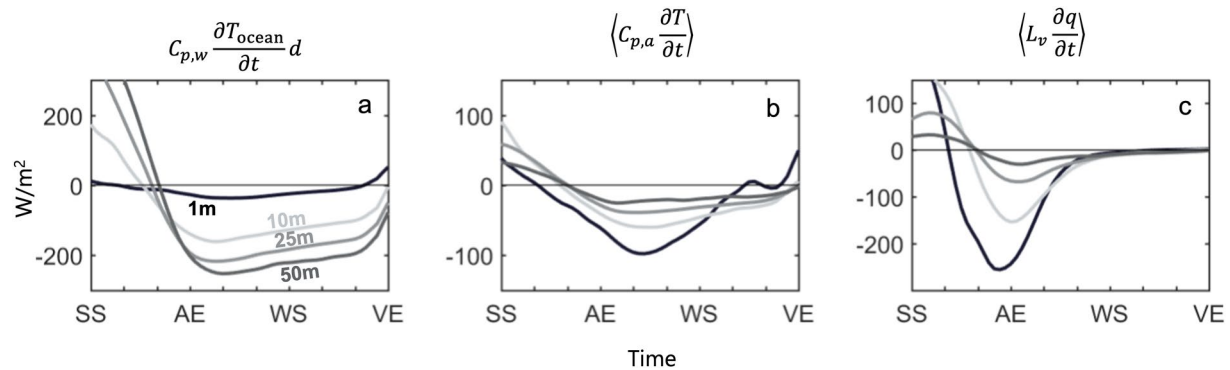


Figure 13. Surface and atmospheric energy storage, as in Figure 8, for 85° simulations with mixed layer depths of 1, 10, 25, and 50 m.

in the high-obliquity simulations and which keeps the poles relatively warm during the winter, hence suppressing eddy formation. These results are largely consistent with the behavior observed in coupled atmosphere–ocean simulations (Ferreira et al., 2014), where the reduction in winter eddy activity at high obliquity was linked to changes in surface temperature gradients. While ocean heat transport played a role in the coupled simulations, the dominant effect was determined to be local ocean heat uptake. These results are also in general agreement with studies of Earth’s climate, which show that surface heat capacity can control the amplitude of midlatitude storm track seasonality by buffering seasonal changes in insolation (Barpanda & Shaw, 2020).

Our aquaplanet simulations, hence, suggest that in Earth-like planets, with a global ocean and a deep mixed layer, the ocean heat storage would control the energy budget and could keep the poles warm enough to weaken or even prevent baroclinic eddy activity. However, it is important to note that the 50 m mixed layer depth also results in a weak seasonal cycle and a weak atmospheric circulation, which implies a weakening of the wind stress and buoyancy forcings that can help sustain a deep mixed layer. Additional future studies with coupled atmospheric and ocean models and a representation of sea ice will be valuable for understanding the ocean’s influence on seasonal behavior and constraining more realistically plausible planetary climate configurations.

6. Discussion and Conclusions

In this study, we have demonstrated the fundamental role that atmospheric moisture plays in mitigating extreme seasonal excursions that one would expect in high-obliquity planets in idealized aquaplanet simulations. One manifestation of this mitigating effect is a weakening or absence of wintertime extratropical baroclinic eddy activity and, with it, of a mid-to-high-latitude precipitating storm track. While a similar behavior was also seen in a previous study using a coupled atmosphere–ocean GCM, and attributed primarily to the large ocean thermal inertia (Ferreira et al., 2014), here we show how this occurs even for very shallow ocean mixed layer depths. The presence of atmospheric moisture increases the effective heat capacity of the atmosphere through its latent energy component, which is a strongly nonlinear function of temperature following the Clausius–Clapeyron relation. This effect reduces summer temperature maxima at the poles. During the fall and winter, the net energy loss in the high latitudes is primarily balanced by latent energy loss, which delays the atmospheric cooling. The condensation that accompanies this atmospheric drying, and the associated latent heat release, counteracts the radiatively driven cooling, slowing down the drop in polar temperatures, and keeping the poles warmer than the low latitudes throughout the winter, which in turn prevents vigorous baroclinic eddy activity that lives off the potential energy stored in the sloping isopycnals.

From an energy budget perspective, the dominant role that latent energy storage and, to a smaller extent, sensible energy storage play in the high latitudes of high-obliquity planets guarantees that energy balance is maintained even with little-to-no atmospheric poleward energy transport in the solstice seasons outside the reach of the broad cross-equatorial winter Hadley cell (Lobo & Bordoni, 2020). It is in fact only at the end of the winter months, when polar temperatures drop significantly, after the atmospheric moisture has been depleted, that baroclinic eddies can form. However, their poleward energy transport is for the most part counteracted by the equatorward energy transported by the resulting Ferrel cell, with overall modest values of net poleward energy transport.

As the ocean mixed layer depth is increased, large seasonal temperature excursions at the high latitudes are buffered by the increasingly larger ocean heat capacity, with energy storage in the ocean surface progressively replacing the atmospheric latent energy storage as the dominant term balancing the net energy loss during the winter months. In this respect, our idealized simulations suggest that regardless of surface thermal inertia, ocean-covered high-obliquity Earth-like planets would not experience significant extratropical storm activity.

Though it is not clear how many rocky planets will feature surface water, any such planets would be immensely appealing targets for habitability studies, given that water is a minimum requirement for life as we know it. As we have shown, the presence of moisture in Earth-like planets can have a significant effect on the atmospheric circulation and its response to changes in radiation. This work, combined with previous studies of lower-latitude features (Lobo & Bordoni, 2020), as well as studies of other planetary regimes including tidally locked planets (Haqq-Misra et al., 2018; Labonté & Merlis, 2020), highlights the importance of accounting for moisture, and its numerous feedbacks, in simulations of planetary climates. While of fundamental importance, the role of water vapor remains challenging to quantify, especially when accounting for cloud processes in more comprehensive GCMs. This was reflected in the TRAPPIST-1 Habitable Atmosphere Intercomparison (THAI) findings (Sergeev et al., 2021), which showed that even without accounting for seasonal variability (obliquity and eccentricity were set to zero) water vapor content led to the largest intermodel differences, as well as in Yang et al. (2019) which included differences based on stellar type. Given the seasonal effects discussed in this work, we strongly recommend future exoplanet intermodel comparisons include planets with strong seasonal cycles.

The use of a slab ocean, with no dynamic coupling and a shallow mixed layer depth, allows us to focus on the atmospheric circulation and its seasonal behavior, thus allowing us to isolate the relevant mechanisms. While it is not meant to be representative of Earth's ocean-covered surfaces, this configuration is both a valuable theoretical tool and potentially a useful representation of land planets and regions with shallow bodies of water. Land planets with various surface water configurations could have wider habitable zones than ocean worlds (Abe et al., 2011; Kodama et al., 2018, 2019), making them attractive targets for further work. In particular, moisture effects discussed in this work could be especially relevant for land planets with surface water concentrated poleward of the Hadley cell edge.

On planets with abundant surface liquid water, we might expect to see expansive and deep Earth-like oceans that would dampen the seasonal cycle. An ocean with substantial heat transport could certainly influence the seasonal climate (Ferreira et al., 2014), as has been shown to be the case even on tidally locked planets (Checlair et al., 2019; Hu & Yang, 2014). But there are few constraints on the abundance of ocean-covered terrestrial exoplanets or their ocean properties. Many factors, including distribution of continents (Salazar et al., 2020), salinity, or sea ice, could significantly affect the ocean's mixed layer depth and thus its ability to store heat locally (Olson et al., 2020). Until further constraints can be placed, it will be important to consider planetary configurations ranging from those dominated by atmospheric transport and storage to those dominated by ocean heat capacity.

Thus far, we have mostly contrasted the effects of atmospheric moisture storage and surface heat capacity on the meridional temperature gradients. But it is worth noting that their combined effects suggest that temperate and moist high-obliquity planets, including ocean-covered worlds and land planets, will likely have weak baroclinicity. It is possible that planet specific properties such as surface albedo and topography could alter these results. For example, an anomalously low polar optical depth could, as we have shown, facilitate temperature gradient reversals. Also, depending on planetary and stellar properties, many of these planets could be susceptible to runaway warming or cooling, potentially leading to a snowball scenario (Shaw & Graham, 2020), resulting in planetary properties far beyond the range of climates considered here. The presence of continents could also significantly complicate these results, changing patterns of surface albedo, heat capacity, and water availability, as has been shown to be relevant for the climate of tidally locked exoplanets (Lewis et al., 2018; Macdonald et al., 2022). Clouds could also play a large role, altering regional optical depth and albedo. But, in the absence of large meridional gradients in planetary properties, on a temperate planet, it is hard to conceive means through which a strong winter Ferrel cell and storm tracks could be sustained in high-obliquity planets.

Strong latent heat effects during seasonal transitions can complicate our understanding of planetary thermal inertia. Significant atmospheric latent heat effects, such as those in our high-obliquity simulations, could delay temperature maxima and minima in the high latitudes, affecting planetary emission patterns, as well as some

atmospheric spectral properties. Previous studies have attempted to relate planetary thermal inertia to changes in light curves (e.g., Cowan et al., 2012; Gaidos & Williams, 2004). But even if we were to overcome observational limitations, atmospheric moisture storage and latent heat effects could make it challenging to distinguish the surface heat capacity's contribution to the planetary thermal inertia.

The relationship between obliquity, planetary thermal emissions, and in particular secondary eclipse properties has been extensively explored for warm Jupiter-sized planets (Ohno & Zhang, 2019b; Rauscher, 2017), in preparation for upcoming *JWST* observations. But for exoplanets with Earth-like planetary and orbital properties, their small size combined with their large orbital radius make observational studies of planetary emissions unachievable in the near future. However, studies of reflected light may become increasingly viable with missions such as *NGRST*, and future versions of *HabEx/LUVOIR*. An Earth twin is still expected to pose a challenge, particularly for water vapor detection (Feng et al., 2018). But for high-obliquity planets, the large seasonal fluctuations in atmospheric water vapor mixing ratio, and albedo changes linked to variations in cloud fraction (not included in our model), could affect the likelihood of water vapor detection.

Also, while water is of particular interest for habitable planets, the mechanisms described here could be relevant for a broader range of planets with other atmospheric constituents that undergo phase changes. For example, methane undergoes phase changes on Titan (Lorenz, 2005) and could play a larger role in Titan-like exoplanets, which are expected to exist around a variety of stellar hosts (Lora et al., 2018).

Data Availability Statement

The data used in this study are available at the Caltech Data Repository, <https://doi.org/10.22002/D1.20050> (Lobo & Bordini, 2022).

Acknowledgments

The simulations were conducted on the Caltech Division of Geological and Planetary Sciences CITerra high performance computing cluster and the Resnick High Performance Computing Cluster. We acknowledge financial support from the Caltech Davidow Discovery Fund.

References

- Abe, Y., Abe-Ouchi, A., Sleep, N. H., & Zahnle, K. J. (2011). Habitable zone limits for dry planets. *Astrobiology*, 11(5), 443–460. <https://doi.org/10.1089/ast.2010.0545>
- Barpanda, P., & Shaw, T. (2017). Using the moist static energy budget to understand storm-track shifts across a range of time scales. *Journal of the Atmospheric Sciences*, 74(8), 2427–2446. <https://doi.org/10.1175/JAS-D-17-0022.1>
- Barpanda, P., & Shaw, T. A. (2020). Surface fluxes modulate the seasonality of zonal-mean storm tracks. *Journal of the Atmospheric Sciences*, 77, 753–779. <https://doi.org/10.1175/JAS-D-19-0139.1>
- Bischoff, T., & Schneider, T. (2014). Energetic constraints on the position of the intertropical convergence zone. *Journal of Climate*, 27(13), 4937–4951. <https://doi.org/10.1175/JCLI-D-13-00650.1>
- Chang, E. K., Lee, S., & Swanson, K. L. (2002). Storm track dynamics. *Journal of Climate*, 15(16), 2163–2183. [https://doi.org/10.1175/1520-0442\(2002\)015<02163:STD>2.0.CO;2](https://doi.org/10.1175/1520-0442(2002)015<02163:STD>2.0.CO;2)
- Checlair, J. H., Olson, S. L., Jansen, M. F., & Abbot, D. S. (2019). No snowball on habitable tidally locked planets with a dynamic ocean. *The Astrophysical Journal*, 884, L46. <https://doi.org/10.3847/2041-8213/ab487d>
- Cowan, N. B., Voigt, A., & Abbot, D. S. (2012). Thermal phases of Earth-like planets: Estimating thermal inertia from eccentricity, obliquity, and diurnal forcing. *The Astrophysical Journal*, 757(1), 80. <https://doi.org/10.1088/0004-637X/757/1/80>
- Cronin, T. W., & Emanuel, K. A. (2013). The climate time scale in the approach to radiative-convective equilibrium. *Journal of Advances in Modeling Earth Systems*, 5, 843–849. <https://doi.org/10.1002/jame.20049>
- Donohoe, A., Frierson, D. M. W., & Battisti, D. S. (2014). The effect of ocean mixed layer depth on climate in slab ocean aquaplanet experiments. *Climate Dynamics*, 43, 1041–1055. <https://doi.org/10.1007/s00382-013-1843-4>
- Faulk, S., Mitchell, J., Bordini, S., Faulk, S., Mitchell, J., & Bordini, S. (2017). Effects of rotation rate and seasonal forcing on the ITCZ extent in planetary atmospheres. *Journal of the Atmospheric Sciences*, 74, 665–678. <https://doi.org/10.1175/JAS-D-16-0014.1>
- Feldl, N., Bordini, S., & Merlis, T. M. (2017). Coupled high-latitude climate feedbacks and their impact on atmospheric heat transport. *Journal of Climate*, 30(1), 189–201. <https://doi.org/10.1175/JCLI-D-16-0324.1>
- Feng, Y. K., Robinson, T. D., Fortney, J. J., Lupu, R. E., Marley, M. S., Lewis, N. K., et al. (2018). Characterizing Earth analogs in reflected light: Atmospheric retrieval studies for future space telescopes. *The Astronomical Journal*, 155, 200. <https://doi.org/10.3847/1538-3881/aab95c>
- Ferreira, D., Marshall, J., O'Gorman, P. A., & Seager, S. (2014). Climate at high-obliquity. *Icarus*, 243, 236–248. <https://doi.org/10.1016/j.icarus.2014.09.015>
- Frierson, D. M. W., Held, I. M., & Zurita-Gotor, P. (2007). A gray-radiation aquaplanet moist GCM. Part II: Energy transports in altered climates. *Journal of the Atmospheric Sciences*, 64(5), 1680–1693. <https://doi.org/10.1175/JAS3913.1>
- Gaidos, E., & Williams, D. M. (2004). Seasonality on terrestrial extrasolar planets: Inferring obliquity and surface conditions from infrared light curves. *New Astronomy*, 10(1), 67–77. <https://doi.org/10.1016/j.newast.2004.04.009>
- Guendelman, I., & Kaspi, Y. (2018). An axisymmetric limit for the width of the Hadley cell on planets with large obliquity and long seasonality. *Geophysical Research Letters*, 45, 13213–13221. <https://doi.org/10.1029/2018GL080752>
- Guendelman, I., & Kaspi, Y. (2019). Atmospheric dynamics on terrestrial planets: The seasonal response to changes in orbital, rotational, and radiative timescales. *The Astrophysical Journal*, 881(1), 67. <https://doi.org/10.3847/1538-4357/ab2a06>
- Haqq-Misra, J., Wolf, E. T., Joshi, M., Zhang, X., & Kopparapu, R. K. (2018). Delineating circulation regimes of synchronously rotating terrestrial planets within the habitable zone. *The Astrophysical Journal*, 852, 67. <https://doi.org/10.3847/1538-4357/aa9f1f>

- Held, I. M. (2001). The partitioning of the poleward energy transport between the tropical ocean and atmosphere. *Journal of the Atmospheric Sciences*, 58(8), 943–948. [https://doi.org/10.1175/1520-0469\(2001\)058<0943:TPOTPE>2.0.CO;2](https://doi.org/10.1175/1520-0469(2001)058<0943:TPOTPE>2.0.CO;2)
- Held, I. M., & Hou, A. Y. (1980). Nonlinear axially symmetric circulations in a nearly inviscid atmosphere. *Journal of the Atmospheric Sciences*, 37, 515–533. [https://doi.org/10.1175/1520-0469\(1980\)037<0515:NASCIA>2.0.CO;2](https://doi.org/10.1175/1520-0469(1980)037<0515:NASCIA>2.0.CO;2)
- Held, I. M., & Soden, B. J. (2000). Water vapor feedback and global warming. *Annual Review of Energy and the Environment*, 25(1), 441–475. <https://doi.org/10.1146/annurev.energy.25.1.441>
- Hu, Y., & Yang, J. (2014). Role of ocean heat transport in climates of tidally locked exoplanets around m dwarf stars. *Proceedings of the National Academy of Sciences of the United States of America*, 111, 629–634. <https://doi.org/10.1073/pnas.1315215111>
- Kaspi, Y., & Showman, A. P. (2015). Atmospheric dynamics of terrestrial exoplanets over a wide range of orbital and atmospheric parameters. *The Astrophysical Journal*, 804(1), 60. <https://doi.org/10.1088/0004-637X/804/1/60>
- Kodama, T., Genda, H., O'ishi, R., Abe-Ouchi, A., & Abe, Y. (2019). Inner edge of habitable zones for Earth-sized planets with various surface water distributions. *Journal of Geophysical Research: Planets*, 124, 2306–2324. <https://doi.org/10.1029/2019JE006037>
- Kodama, T., Nitta, A., Genda, H., Takao, Y., O'ishi, R., Abe-Ouchi, A., & Abe, Y. (2018). Dependence of the onset of the runaway greenhouse effect on the latitudinal surface water distribution of Earth-like planets. *Journal of Geophysical Research: Planets*, 123, 559–574. <https://doi.org/10.1002/2017JE005383>
- Labonté, M.-P., & Merlis, T. M. (2020). Sensitivity of the atmospheric water cycle within the habitable zone of a tidally locked, Earth-like exoplanet. *The Astrophysical Journal*, 896, 31. <https://doi.org/10.3847/1538-4357/ab9102>
- Lapeyre, G., & Held, I. M. (2004). The role of moisture in the dynamics and energetics of turbulent baroclinic eddies. *Journal of the Atmospheric Sciences*, 61(14), 1693–1710. [https://doi.org/10.1175/1520-0469\(2004\)061<1693:TROMIT>2.0.CO;2](https://doi.org/10.1175/1520-0469(2004)061<1693:TROMIT>2.0.CO;2)
- Lewis, N. T., Lambert, F. H., Boutle, I. A., Mayne, N. J., Manners, J., & Acreman, D. M. (2018). The influence of a substellar continent on the climate of a tidally locked exoplanet. *The Astrophysical Journal*, 854, 171. <https://doi.org/10.3847/1538-4357/aaad0a>
- Lindzen, R. S., & Hou, A. V. (1988). Hadley circulations for zonally averaged heating centered off the equator. *Journal of the Atmospheric Sciences*, 45(17), 2416–2427. [https://doi.org/10.1175/1520-0469\(1988\)045<2416:HCFZAH>2.0.CO;2](https://doi.org/10.1175/1520-0469(1988)045<2416:HCFZAH>2.0.CO;2)
- Lobo, A. H., & Bordini, S. (2020). Atmospheric dynamics in high obliquity planets. *Icarus*, 340, 113592. <https://doi.org/10.1016/j.icarus.2019.113592>
- Lobo, A. H., & Bordini, S. (2022). Idealized simulations of Earth-like planets. CaltechDATA [Dataset]. <https://doi.org/10.22002/D1.20050>
- Lora, J. M., Kataria, T., & Gao, P. (2018). Atmospheric circulation, chemistry, and infrared spectra of titan-like exoplanets around different stellar types. *The Astrophysical Journal*, 853, 58. <https://doi.org/10.3847/1538-4357/aaa132>
- Lorenz, R. D. (2005). Convective plumes and the scarcity of Titan's clouds. *Geophysical Research Letters*, 32, L01201. <https://doi.org/10.1029/2004GL021415>
- Macdonald, E., Paradise, A., Menou, K., & Lee, C. (2022). Climate uncertainties caused by unknown land distribution on habitable m-Earths. *Monthly Notices of the Royal Astronomical Society*, 513, 2761–2769. <https://doi.org/10.1093/mnras/stac1040>
- McGee, D., Donohoe, A., Marshall, J., & Ferreira, D. (2014). Changes in ITCZ location and cross-equatorial heat transport at the Last Glacial Maximum, Heinrich Stadial 1, and the mid-Holocene. *Earth and Planetary Science Letters*, 390, 69–79. <https://doi.org/10.1016/j.epsl.2013.12.043>
- Merlis, T. M., & Schneider, T. (2010). Atmospheric dynamics of Earth-like tidally locked aquaplanets. *Journal of Advances in Modeling Earth Systems*, 2, 13. <https://doi.org/10.3894/JAMES.2010.2.13>
- Miguel, Y., & Brunini, A. (2010). Planet formation: Statistics of spin rates and obliquities of extrasolar planets. *Monthly Notices of the Royal Astronomical Society*, 406, 1935–1943. <https://doi.org/10.1111/j.1365-2966.2010.16804.x>
- Mitchell, J. L., Pierrehumbert, R. T., Frierson, D. M., & Caballero, R. (2009). The impact of methane thermodynamics on seasonal convection and circulation in a model Titan atmosphere. *Icarus*, 203(1), 250–264. <https://doi.org/10.1016/j.icarus.2009.03.043>
- Neelin, J. D. (2007). Moist dynamics of tropical convection zones in monsoons, teleconnections and global warming. In T. Schneider & A. H. Sobel (Eds.), *The global circulation of the atmosphere* (pp. 267–301). Princeton, NJ: Princeton University Press.
- Neelin, J. D., & Held, I. M. (1987). Modeling tropical convergence based on the moist static energy budget. *Monthly Weather Review*, 115(1), 3–12. [https://doi.org/10.1175/1520-0493\(1987\)115<0003:MTCBOT>2.0.CO;2](https://doi.org/10.1175/1520-0493(1987)115<0003:MTCBOT>2.0.CO;2)
- O'Gorman, P. A. (2011). The effective static stability experienced by eddies in a moist atmosphere. *Journal of the Atmospheric Sciences*, 68(1), 75–90. <https://doi.org/10.1175/2010JAS3537.1>
- O'Gorman, P. A., & Schneider, T. (2008). The hydrological cycle over a wide range of climates simulated with an idealized GCM. *Journal of Climate*, 21, 3815–3832. <https://doi.org/10.1175/2007JCLI2065.1>
- Ohno, K., & Zhang, X. (2019a). Atmospheres on nonsynchronized eccentric-tilted exoplanets. I. Dynamical regimes. *The Astrophysical Journal*, 874, 1. <https://doi.org/10.3847/1538-4357/ab06cc>
- Ohno, K., & Zhang, X. (2019b). Atmospheres on nonsynchronized eccentric-tilted exoplanets. II. Thermal light curves. *The Astrophysical Journal*, 874, 2. <https://doi.org/10.3847/1538-4357/ab06ca>
- Olson, S. L., Jansen, M., & Abbot, D. S. (2020). Oceanographic considerations for exoplanet life detection. *The Astrophysical Journal*, 895(1), 19. <https://doi.org/10.3847/1538-4357/ab88c9>
- Peixoto, J. P., & Oort, A. H. (1992). *Physics of climate*. New York, NY: American Institute of Physics.
- Pfahl, S., O'Gorman, P. A., & Singh, M. S. (2015). Extratropical cyclones in idealized simulations of changed climates. *Journal of Climate*, 28(23), 9373–9392. <https://doi.org/10.1175/JCLI-D-14-00816.1>
- Pierrehumbert, R. T., & Swanson, K. L. (1995). Baroclinic instability. *Annual Review of Fluid Mechanics*, 27, 419–467. <https://doi.org/10.1146/annurev.fl.27.010195.002223>
- Rauscher, E. (2017). Models of warm Jupiter atmospheres: Observable signatures of obliquity. *The Astrophysical Journal*, 846, 69. <https://doi.org/10.3847/1538-4357/aa81c3>
- Salazar, A. M., Olson, S. L., Komacek, T. D., Stephens, H., & Abbot, D. S. (2020). The effect of substellar continent size on ocean dynamics of Proxima Centauri b. *The Astrophysical Journal*, 896, L16. <https://doi.org/10.3847/2041-8213/ab94c1>
- Schneider, T., & Walker, C. C. (2006). Self-organization of atmospheric macroturbulence into critical states of weak nonlinear eddy–eddy interactions. *Journal of the Atmospheric Sciences*, 63(6), 1569–1586. <https://doi.org/10.1175/JAS3699.1>
- Sergeev, D. E., Fauchez, T. J., Turbet, M., Boutle, I. A., Tsigaridis, K., Way, M. J., et al. (2021). The TRAPPIST-1 Habitable Atmosphere Inter-comparison (THAI). Part II: Moist cases—The two waterworlds. *arXiv*. <https://doi.org/10.48550/arXiv.2109.11459>
- Shaw, T. A., & Graham, R. J. (2020). Hydrological cycle changes explain weak snowball Earth storm track despite increased surface baroclinicity. *Geophysical Research Letters*, 47, e2020GL089866. <https://doi.org/10.1029/2020GL089866>
- Showman, A. P., Wordsworth, R. D., Merlis, T. M., & Kaspi, Y. (2013). Atmospheric circulation of terrestrial exoplanets. In *Comparative climatology of terrestrial planets*. Tucson, AZ: University of Arizona Press. https://doi.org/10.2458/azu_uapress_9780816530595-ch12

- Stone, P. H. (1978). Baroclinic adjustment. *Journal of the Atmospheric Sciences*, 35, 561–571. [https://doi.org/10.1175/1520-0469\(1978\)035<0561:BA>2.0.CO;2](https://doi.org/10.1175/1520-0469(1978)035<0561:BA>2.0.CO;2)
- Tan, Z., Lachmy, O., & Shaw, T. A. (2019). The sensitivity of the jet stream response to climate change to radiative assumptions. *Journal of Advances in Modeling Earth Systems*, 11, 934–956. <https://doi.org/10.1029/2018MS001492>
- Wolf, E. T., Shields, A. L., Kopparapu, R. K., Haqq-Misra, J., & Toon, O. B. (2017). Constraints on climate and habitability for Earth-like exoplanets determined from a general circulation model. *The Astrophysical Journal*, 837(2), 107. <https://doi.org/10.3847/1538-4357/aa5ffc>
- Yang, J., Leconte, J., Wolf, E. T., Merlis, T., Koll, D. D. B., Forget, F., & Abbot, D. S. (2019). Simulations of water vapor and clouds on rapidly rotating and tidally locked planets: A 3D model intercomparison. *The Astrophysical Journal*, 875, 46. <https://doi.org/10.3847/1538-4357/ab09f1>